High p_T direct photon and π^0 triggered azimuthal jet correlations and measurement of k_T for isolated direct photons in $p + p$ collisions at $\sqrt{s} = 200$ GeV

A. Adare,[11] S. Afanasiev,[25] C. Aidala,[12,36] N. N. Ajitanand,[53] Y. Akiba,[47,48] H. Al-Bataineh,[42] J. Alexander,[53] K. Aoki,[30,47] L. Aphecetche,[55] R. Armendariz,[42] S. H. Aronson,[6] J. Asai,[47,48] E. T. Atomssa,[31] R. Averbeck,[54] T. C. Awes,[43] B. Azmoun,[6] V. Babintsev,[21] M. Bai,[5] G. Baksay,[17] L. Baksay,[17] A. Baldisseri,[14] K. N. Barish,[7] P. D. Barnes,[33] B. Bassalleck,[41] A. T. Basye,[1] S. Bathe,[7] S. Batsouli,[43] V. Baublis,[46] C. Baumann,[37] A. Bazilevsky,[6] S. Belikov,[6,*] R. Bennett,[54] A. Berdnikov,[50] Y. Berdnikov,[50] A. A. Bickley,[11] J. G. Boissevain,[33] H. Borel,[14] K. Boyle,[54] M. L. Brooks,[33] H. Buesching,[6] V. Bumazhnov,[21] G. Bunce,[6,48] S. Butsyk,[33,54] C. M. Camacho,[33] S. Campbell,[54] B. S. Chang,[62] W. C. Chang,[2] J.-L. Charvet,[14] S. Chernichenko,[21] J. Chiba,[26] C. Y. Chi,[12] M. Chiu,[22] I. J. Choi,[62] R. K. Choudhury,[4] T. Chujo,[58,59] P. Chung,[53] A. Churyn,[21] V. Cianciolo,[43] Z. Citron,[54] C. R. Cleven,[19] B. A. Cole,[12] M. P. Comets,[44] M. Connors,[54] P. Constantin,[33] M. Csanád,[16] T. Csörgő,[27] T. Dahms,[54] S. Dairaku,[30,47] K. Das,[18] G. David,[6] M. B. Deaton,[1] K. Dehmelt,[17] H. Delagrange,[55] A. Denisov,[21] D. d'Enterria,[12,31] A. Deshpande,[48,54] E. J. Desmond,[6] O. Dietzsch,[51] A. Dion,[54] M. Donadelli,[51] O. Drapier,[31] A. Drees,[54] K. A. Drees,[5] A. K. Dubey,[61] A. Durum,[21] D. Dutta,[4] V. Dzhordzhadze,[7] Y. V. Efremenko,[43] J. Egdemir,[54] F. Ellinghaus,[11] W. S. Emam,[7] T. Engelmore,[12] A. Enokizono,[32] H. En'yo,[47,48] S. Esumi,[58] K. O. Eyser,[7] B. Fadem,[38] D. E. Fields,[41,48] M. Finger, Jr.,[8,25] M. Finger,[8,25] F. Fleuret,[31] S. L. Fokin,[29] Z. Fraenkel,[61,*] J. E. Frantz,[54] A. Franz,[6] A. D. Frawley,[18] K. Fujiwara,[47] Y. Fukao,[30,47] T. Fusayasu,[40] S. Gadrat,[34] I. Garishvili,[56] A. Glenn,[11] H. Gong,[54] M. Gonin,[31] J. Gosset,[14] Y. Goto,[47,48] R. Granier de Cassagnac,[31] N. Grau,[12,24] S. V. Greene,[59] M. Grosse Perdekamp,[22,48] T. Gunji,[10] H.-Å. Gustafsson,[35,*] T. Hachiya,[20] A. Hadj Henni,[55] C. Haegemann,[41] J. S. Haggerty,[6] H. Hamagaki,[10] R. Han,[45] H. Harada,[20] E. P. Hartouni,[32] K. Haruna,[20] E. Haslum,[35] R. Hayano,[10] M. Heffner,[32] T. K. Hemmick,[54] T. Hester,[7] X. He,[19] H. Hiejima,[22] J. C. Hill,[24] R. Hobbs,[41] M. Hohlmann,[17] W. Holzmann,[53] K. Homma,[20] B. Hong,[28] T. Horaguchi,[10,47,57] D. Hornback,[56] S. Huang,[59] T. Ichihara,[47,48] R. Ichimiya,[47] H. Iinuma,[30,47] Y. Ikeda,[58] K. Imai,[30,47] J. Imrek,[15] M. Inaba,[58] Y. Inoue,[49,47] D. Isenhower,[1] L. Isenhower,[1] M. Ishihara,[47] T. Isobe,[10] M. Issah,[53] A. Isupov,[25] D. Ivanischev,[46] B. V. Jacak,[54,†] J. Jia,[12] J. Jin,[12] O. Jinnouchi,[48] B. M. Johnson,[6] K. S. Joo,[39] D. Jouan,[44] F. Kajihara,[10] S. Kametani,[10,47,60] N. Kamihara,[47,48] J. Kamin,[54] M. Kaneta,[48] J. H. Kang,[62] H. Kanou,[47,57] J. Kapustinsky,[33] D. Kawall,[36,48] A. V. Kazantsev,[29] T. Kempel,[24] A. Khanzadeev,[46] K. M. Kijima,[20] J. Kikuchi,[60] B. I. Kim,[28] D. H. Kim,[39] D. J. Kim,[62] E. Kim,[52] S. H. Kim,[62] E. Kinney,[11] K. Kiriluk,[11] Á. Kiss,[16] E. Kistenev,[6] A. Kiyomichi,[47] J. Klay,[32] C. Klein-Boesing,[37] L. Kochenda,[46] V. Kochetkov,[21] B. Komkov,[46] M. Konno,[58] J. Koster,[22] D. Kotchetkov,[7] A. Kozlov,[61] A. Král,[13] A. Kravitz,[12] J. Kubart,[8,23] G. J. Kunde,[33] N. Kurihara,[10] K. Kurita,[49,47] M. Kurosawa,[47] M. J. Kweon,[28] Y. Kwon,[56,62] G. S. Kyle,[42] R. Lacey,[53] Y. S. Lai,[12] J. G. Lajoie,[24] D. Layton,[22] A. Lebedev,[24] D. M. Lee,[33] K. B. Lee,[28] M. K. Lee,[62] T. Lee,[52] M. J. Leitch,[33] M. A. L. Leite,[51] B. Lenzi,[51] P. Liebing,[48] T. Liška,[13] A. Litvinenko,[25] H. Liu,[42] M. X. Liu,[33] X. Li,[9] B. Love,[59] D. Lynch,[6] C. F. Maguire,[59] Y. I. Makdisi,[5] A. Malakhov,[25] M. D. Malik,[41] V. I. Manko,[29] E. Mannel,[12] Y. Mao,[45,47] L. Mašek,[8,23] H. Masui,[58] F. Matathias,[12] M. McCumber,[54] P. L. McGaughey,[33] N. Means,[54] B. Meredith,[22] Y. Miake,[58] P. Mikeš,[8,23] K. Miki,[58] T. E. Miller,[59] A. Milov,[6,54] S. Mioduszewski,[6] M. Mishra,[3] J. T. Mitchell,[6] M. Mitrovski,[53] A. K. Mohanty,[4] Y. Morino,[10] A. Morreale,[7] D. P. Morrison,[6] T. V. Moukhanova,[29] D. Mukhopadhyay,[59] J. Murata,[49,47] S. Nagamiya,[26] Y. Nagata,[58] J. L. Nagle,[11] M. Naglis,[61] M. I. Nagy,[16] I. Nakagawa,[47,48] Y. Nakamiya,[20] T. Nakamura,[20] K. Nakano,[47,57] J. Newby,[32] M. Nguyen,[54] T. Niita,[58] B. E. Norman,[33] R. Nouicer,[6] A. S. Nyanin,[29] E. O'Brien,[6] S. X. Oda,[10] C. A. Ogilvie,[24] H. Ohnishi,[47] K. Okada,[48] M. Oka,[58] O. O. Omiwade,[1] Y. Onuki,[47] A. Oskarsson,[35] M. Ouchida,[20] K. Ozawa,[10] R. Pak,[6] D. Pal,[59] A. P. T. Palounek,[33] V. Pantuev,[54] V. Papavassiliou,[42] J. Park,[52] W. J. Park,[28] S. F. Pate,[42] H. Pei,[24] J.-C. Peng,[22] H. Pereira,[14] V. Peresedov,[25] D. Yu. Peressounko,[29] C. Pinkenburg,[6] M. L. Purschke,[6] A. K. Purwar,[33] H. Qu,[19] J. Rak,[41] A. Rakotozafindrabe,[31] I. Ravinovich,[61] K. F. Read,[43,56] S. Rembeczki,[17] M. Reuter,[54] K. Reygers,[37] V. Riabov,[46] Y. Riabov,[46] D. Roach,[59] G. Roche,[34] S. D. Rolnick,[7] A. Romana,[31,*] M. Rosati,[24] S. S. E. Rosendahl,[35] P. Rosnet,[34] P. Rukoyatkin,[25] P. Ružička,[23] V. L. Rykov,[47] B. Sahlmueller,[37] N. Saito,[30,47,48] T. Sakaguchi,[6] S. Sakai,[58] K. Sakashita,[47,57] H. Sakata,[20] V. Samsonov,[46] S. Sato,[26] T. Sato,[58] S. Sawada,[26] K. Sedgwick,[7] J. Seele,[11] R. Seidl,[22] A. Yu. Semenov,[24] V. Semenov,[21] R. Seto,[7] D. Sharma,[61] I. Shein,[21] A. Shevel,[46,53] T.-A. Shibata,[47,57] K. Shigaki,[20] M. Shimomura,[58] K. Shoji,[30,47] P. Shukla,[4] A. Sickles,[6,54] C. L. Silva,[51] D. Silvermyr,[43] C. Silvestre,[14] K. S. Sim,[28] B. K. Singh,[3] C. P. Singh,[3] V. Singh,[3] S. Skutnik,[24] M. Slunečka,[8,25] A. Soldatov,[21] R. A. Soltz,[32] W. E. Sondheim,[33] S. P. Sorensen,[56] I. V. Sourikova,[6] F. Staley,[14] P. W. Stankus,[43] E. Stenlund,[35] M. Stepanov,[42] A. Ster,[27] S. P. Stoll,[6] T. Sugitate,[20] C. Suire,[44] A. Sukhanov,[6] J. Sziklai,[27] T. Tabaru,[48] S. Takagi,[58] E. M. Takagui,[51] A. Taketani,[47,48] R. Tanabe,[58] Y. Tanaka,[40] S. Taneja,[54] K. Tanida,[47,48,52] M. J. Tannenbaum,[6] A. Taranenko,[53] P. Tarján,[15] H. Themann,[54]

T. L. Thomas,[41] M. Togawa,[30,47] A. Toia,[54] J. Tojo,[47] L. Tomášek,[23] Y. Tomita,[58] H. Torii,[20,47] R. S. Towell,[1] V-N. Tram,[31]
I. Tserruya,[61] Y. Tsuchimoto,[20] C. Vale,[24] H. Valle,[59] H. W. van Hecke,[33] A. Veicht,[22] J. Velkovska,[59] R. Vértesi,[15]
A. A. Vinogradov,[29] M. Virius,[13] V. Vrba,[23] E. Vznuzdaev,[46] M. Wagner,[30,47] D. Walker,[54] X. R. Wang,[42] Y. Watanabe,[47,48]
F. Wei,[24] J. Wessels,[37] S. N. White,[6] D. Winter,[12] C. L. Woody,[6] M. Wysocki,[11] W. Xie,[48] Y. L. Yamaguchi,[60]
K. Yamaura,[20] R. Yang,[22] A. Yanovich,[21] Z. Yasin,[7] J. Ying,[19] S. Yokkaichi,[47,48] G. R. Young,[43] I. Younus,[41]
I. E. Yushmanov,[29] W. A. Zajc,[12] O. Zaudtke,[37] C. Zhang,[43] S. Zhou,[9] J. Zimányi,[27,*] and L. Zolin[25]

(PHENIX Collaboration)

[1]*Abilene Christian University, Abilene, Texas 79699, USA*
[2]*Institute of Physics, Academia Sinica, Taipei 11529, Taiwan*
[3]*Department of Physics, Banaras Hindu University, Varanasi 221005, India*
[4]*Bhabha Atomic Research Centre, Bombay 400 085, India*
[5]*Collider-Accelerator Department, Brookhaven National Laboratory, Upton, New York 11973-5000, USA*
[6]*Physics Department, Brookhaven National Laboratory, Upton, New York 11973-5000, USA*
[7]*University of California—Riverside, Riverside, California 92521, USA*
[8]*Charles University, Ovocný trh 5, Praha 1, 116 36, Prague, Czech Republic*
[9]*China Institute of Atomic Energy (CIAE), Beijing, People's Republic of China*
[10]*Center for Nuclear Study, Graduate School of Science, University of Tokyo, 7-3-1 Hongo, Bunkyo, Tokyo 113-0033, Japan*
[11]*University of Colorado, Boulder, Colorado 80309, USA*
[12]*Columbia University, New York, New York 10027 and Nevis Laboratories, Irvington, New York 10533, USA*
[13]*Czech Technical University, Zikova 4, 166 36 Prague 6, Czech Republic*
[14]*Dapnia, CEA Saclay, F-91191, Gif-sur-Yvette, France*
[15]*Debrecen University, H-4010 Debrecen, Egyetem tér 1, Hungary*
[16]*ELTE, Eötvös Loránd University, H - 1117 Budapest, Pázmány P. s. 1/A, Hungary*
[17]*Florida Institute of Technology, Melbourne, Florida 32901, USA*
[18]*Florida State University, Tallahassee, Florida 32306, USA*
[19]*Georgia State University, Atlanta, Georgia 30303, USA*
[20]*Hiroshima University, Kagamiyama, Higashi-Hiroshima 739-8526, Japan*
[21]*IHEP Protvino, State Research Center of Russian Federation, Institute for High Energy Physics, Protvino, 142281, Russia*
[22]*University of Illinois at Urbana–Champaign, Urbana, Illinois 61801, USA*
[23]*Institute of Physics, Academy of Sciences of the Czech Republic, Na Slovance 2, 182 21 Prague 8, Czech Republic*
[24]*Iowa State University, Ames, Iowa 50011, USA*
[25]*Joint Institute for Nuclear Research, 141980 Dubna, Moscow Region, Russia*
[26]*KEK, High Energy Accelerator Research Organization, Tsukuba, Ibaraki 305-0801, Japan*
[27]*KFKI Research Institute for Particle and Nuclear Physics of the Hungarian Academy of Sciences (MTA KFKI RMKI),
H-1525 Budapest 114, PO Box 49, Budapest, Hungary*
[28]*Korea University, Seoul 136-701, Korea*
[29]*Russian Research Center "Kurchatov Institute," Moscow, Russia*
[30]*Kyoto University, Kyoto 606-8502, Japan*
[31]*Laboratoire Leprince-Ringuet, Ecole Polytechnique, CNRS-IN2P3, Route de Saclay, F-91128, Palaiseau, France*
[32]*Lawrence Livermore National Laboratory, Livermore, California 94550, USA*
[33]*Los Alamos National Laboratory, Los Alamos, New Mexico 87545, USA*
[34]*LPC, Université Blaise Pascal, CNRS-IN2P3, Clermont-Fd, 63177 Aubiere Cedex, France*
[35]*Department of Physics, Lund University, Box 118, SE-221 00 Lund, Sweden*
[36]*Department of Physics, University of Massachusetts, Amherst, Massachusetts 01003-9337, USA*
[37]*Institut für Kernphysik, University of Muenster, D-48149 Muenster, Germany*
[38]*Muhlenberg College, Allentown, Pennsylvania 18104-5586, USA*
[39]*Myongji University, Yongin, Kyonggido 449-728, Korea*
[40]*Nagasaki Institute of Applied Science, Nagasaki-shi, Nagasaki 851-0193, Japan*
[41]*University of New Mexico, Albuquerque, New Mexico 87131, USA*
[42]*New Mexico State University, Las Cruces, New Mexico 88003, USA*
[43]*Oak Ridge National Laboratory, Oak Ridge, Tennessee 37831, USA*
[44]*IPN-Orsay, Universite Paris Sud, CNRS-IN2P3, BP1, F-91406, Orsay, France*
[45]*Peking University, Beijing, People's Republic of China*
[46]*PNPI, Petersburg Nuclear Physics Institute, Gatchina, Leningrad region, 188300, Russia*
[47]*RIKEN Nishina Center for Accelerator-Based Science, Wako, Saitama 351-0198, Japan*
[48]*RIKEN BNL Research Center, Brookhaven National Laboratory, Upton, New York 11973-5000, USA*
[49]*Physics Department, Rikkyo University, 3-34-1 Nishi-Ikebukuro, Toshima, Tokyo 171-8501, Japan*

[50]*Saint Petersburg State Polytechnic University, St. Petersburg, Russia*
[51]*Universidade de São Paulo, Instituto de Física, Caixa Postal 66318, São Paulo CEP05315-970, Brazil*
[52]*Seoul National University, Seoul 151-742, Korea*
[53]*Chemistry Department, Stony Brook University, SUNY, Stony Brook, New York 11794-3400, USA*
[54]*Department of Physics and Astronomy, Stony Brook University, SUNY, Stony Brook, New York 11794, USA*
[55]*SUBATECH (Ecole des Mines de Nantes, CNRS-IN2P3, Université de Nantes) BP 20722 - 44307, Nantes, France*
[56]*University of Tennessee, Knoxville, Tennessee 37996, USA*
[57]*Department of Physics, Tokyo Institute of Technology, Oh-okayama, Meguro, Tokyo 152-8551, Japan*
[58]*Institute of Physics, University of Tsukuba, Tsukuba, Ibaraki 305, Japan*
[59]*Vanderbilt University, Nashville, Tennessee 37235, USA*
[60]*Waseda University, Advanced Research Institute for Science and Engineering, 17 Kikui-cho, Shinjuku-ku, Tokyo 162-0044, Japan*
[61]*Weizmann Institute, Rehovot 76100, Israel*
[62]*Yonsei University, IPAP, Seoul 120-749, Korea*

Correlations of charged hadrons of $1 < p_T < 10$ Gev/c with high p_T direct photons and π^0 mesons in the range $5 < p_T < 15$ Gev/c are used to study jet fragmentation in the γ + jet and dijet channels, respectively. The magnitude of the partonic transverse momentum, k_T, is obtained by comparing to a model incorporating a Gaussian k_T smearing. The sensitivity of the associated charged hadron spectra to the underlying fragmentation function is tested and the data are compared to calculations using recent global fit results. The shape of the direct photon-associated hadron spectrum as well as its charge asymmetry are found to be consistent with a sample dominated by quark-gluon Compton scattering. No significant evidence of fragmentation photon correlated production is observed within experimental uncertainties.

I. INTRODUCTION

Direct photon production in $p + p$ collisions has long been regarded as a fundamental observable [1]. At leading order (LO) in perturbative quantum chromodynamics (pQCD) photons are produced directly from the hard scattering of partons and are hence independent of nonperturbative effects from hadronization. The LO diagrams, shown in Fig. 1, arise from two parton scattering processes: quark-gluon Compton scattering and quark antiquark annihilation. Figure 2 (upper panel) shows the fractional contribution of leading order parton scattering processes for $\sqrt{s} = 200$ GeV $p + p$ collisions at midrapidity ($|\eta| < 0.35$) using the CTEQ6 parton distribution functions [2]. Compton scattering dominates due to the abundance of gluons relative to antiquarks. Because of the preponderance of gluons in the initial state, direct photons have historically been used to probe the gluon distribution of the proton [3,4]. For comparison, Fig. 2 (lower panel) shows the contributing processes to leading order dijet production using a hadron trigger, in this case a π^0. Their relative contributions have a nontrivial p_T dependence, in large part a consequence of triggering on a jet fragment.[1] In the final state, to the extent that leading order Compton scattering dominates, the direct photon is likely to oppose a quark jet. Moreover, the transverse momentum

of the recoil parton is exactly nominally balanced by that of the photon, a feature often exploited to determine the energy scale in jet reconstruction [6].

Beyond LO, photons may be produced by bremsstrahlung from a quark. Although the rate for hard photon radiation is calculable at next-to-leading order (NLO), photons must be considered part of the jet below an arbitrary fragmentation scale. The contribution of these fragmentation photons depends on the nonperturbative parton-to-photon fragmentation functions which are poorly constrained relative to the fragmentation functions into hadrons [7,8]. NLO effects spoil the exact transverse momentum balance between the photon and the recoil jet which holds at LO. Often the contribution from fragmentation photons is suppressed by applying an isolation criterion to the photon sample [9–13]. Typically, the total energy from hadron production in a cone around the photon is required to be small compared to that of the photon. The cross section of isolated photons may then be compared to NLO calculations with the same isolation criterion applied.

At LO, a pair of hard-scattered partons emerges exactly back-to-back. However, due to the finite size of the proton, each of the colliding partons has a small transverse momentum on the order of 300 MeV [14]. At NLO, an additional transverse momentum component arises from emission of a parton in the initial state. Effects that give rise to a nonzero p_T^{pair}, defined as the vector sum of the outgoing parton transverse momenta, are collectively referred to as the k_T effect, $\vec{k}_T$ being defined as the transverse

---

*Deceased.

[†]jacak@skipper.physics.sunysb.edu (PHENIX spokesperson).

[1]The KKP fragmentation functions [5] were used in this example.

FIG. 1.   Leading order Feynman diagrams contributing to direct photon production. From left to right: *s* and *u* channel quark-gluon Compton scattering and *t* and *u* channel quark antiquark annihilation.

momentum per parton ($|k_T| = |p_T^{\text{pair}}|/\sqrt{2}$). The component of k_T in the direction transverse to the outgoing parton pair causes them to be acoplanar while the component along the axis of the outgoing parton pair imparts to them a momentum imbalance.

For observables such as Drell-Yan production, NLO calculations are insufficient to describe the magnitude of the k_T effect, since multiple soft gluon emission gives an additional contribution requiring a resummation of the perturbative series [15]. Measurements of $\langle p_T^{\text{pair}} \rangle$ show
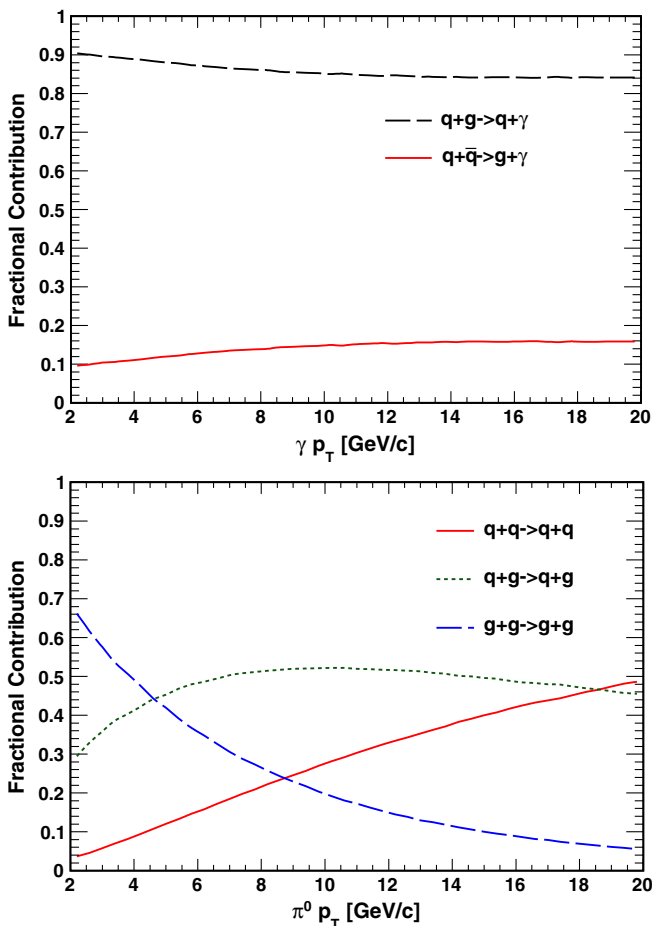
comparable values for Drell-Yan, dijet and diphoton events many of which are compiled in Fig. 30 of [16].

It was argued in [17] that NLO pQCD is insufficient to describe the world data on direct photon cross sections. This claim was contested in [18] in which it was argued that inconsistencies among the data sets may instead be responsible for discrepancies between data and NLO. Although progress has been made, most notably in the form of the joint-resummation approach [19], there is not yet a resummed theory which successfully describes all the data. As a consequence, direct photon data are not used in most determinations of the parton distribution functions.

Direct photons are also an important observable in heavy-ion collisions [20]. A wealth of evidence indicates that a hot, dense state of matter characterized by partonic degrees of freedom is produced in these collisions [21]. Hard-scattered partons are believed to rapidly lose their energy to this QCD medium based on the observation of the suppression of high-p_T hadrons [22,23], a phenomenon known as jet quenching. At LO, direct photons play the role of the hard-scattered parton (see Fig. 1) with the distinction that, as color-neutral objects, they do not interact strongly with the hot QCD matter. The absence of any nuclear modification for direct photons [24] therefore acts as a control measurement for the jet quenching phenomenon and constrains possible contributions from novel sources of induced photon production predicted to arise from the interaction of partons with the QCD medium [25,26].

Just as photons may be used to determine the jet energy scale in $p + p$ collisions, they may be used to estimate, on an event-by-event basis, the initial energy of the opposite-side parton in heavy-ion collisions, an idea first proposed in [27]. The distribution of hadrons in the away-side jet reflects the so-called medium-modified fragmentation function which is the product of the jet fragmentation in the dense QCD environment. Deviations from vacuum jet fragmentation, as observed in $p + p$ collisions, hence should enable tomographic studies of the medium using the energy loss of the away side to probe the density profile of the medium. A first, albeit statistics-limited measurement, of direct photon-hadron correlations was presented in [28]. For a recent review of medium-modified fragmentation functions the reader is referred to [29].

The interpretation of direct photon-triggered correlations in heavy-ion collisions necessitates detailed measurements of such correlations in $p + p$ collisions. The

FIG. 2 (color online).   The fractional contribution of parton scattering processes to (upper panel) inclusive direct photon and (lower panel) π^0 production at LO in $p + p$ collisions at $\sqrt{s} = 200$ GeV. The processes $q + \bar{q} \rightarrow g + g$ and $g + g \rightarrow q + \bar{q}$ contribute to π^0 triggered events at the level of approximately 1% and 0.01%, respectively, and are not shown.

momentum balance between the photon and the opposite-side parton is spoiled due the k_T effect and by the contribution of fragmentation photons in the direct photon sample. The present work endeavors to study such effects. The remainder of the article is organized as follows. In Sec. II we describe elements of the apparatus relevant to the measurement of photon-hadron correlations. In Sec. III the methodology of extracting direct photon correlations from the background of decay photon-hadron correlations is detailed. Section IV presents results on π^0 and direct photon-triggered correlations. Finally, Sec. V interprets the results at the partonic level using a LO pQCD calculation coupled with phenomenologically motivated k_T smearing.

II. DETECTOR DESCRIPTION AND PARTICLE IDENTIFICATION

A. The PHENIX detector

The PHENIX detector, described in [30], is well suited for jet correlations between photons and hadrons. The central arms of the detector are nearly back-to-back in azimuth (offset by 22.5°), each subtending 90° and covering 0.7 units of pseudorapidity around midrapidity. Each arm contains charged particle tracking chambers and electromagnetic calorimeters [31].

The electromagnetic calorimeters (EMCal) [32] consist of two types of detectors, six sectors of lead-scintillator (PbSc) sampling calorimeters and two of lead-glass (PbGl) Čerenkov calorimeters, which measure electromagnetic showers with intrinsic resolution $\sigma_E/E = 2.1\% \oplus 8.1\%/\sqrt{E}$ and $0.8\% \oplus 5.9\%/\sqrt{E}$, respectively. The fine segmentation of the EMCal ($\Delta\eta \times \Delta\phi \sim 0.01 \times 0.01$ for PbSc and $\sim 0.008 \times 0.008$ for PbGl) allows for π^0 reconstruction in the diphoton decay channel out to $p_T > 20$ GeV/c. In order to measure direct photons over the range $5 < p_T < 15$ GeV/c, π^0 and η must be reconstructed over a larger range of $4 < p_T < 17$ GeV/c to account for decay feed-down and detector resolution as described below. Direct photon, π^0 and η cross section measurements in $p + p$ collisions are described in [33–35]. Photon candidates of very high purity ($> 98\%$ for energies >5 GeV) are selected from EMCal clusters with the use of cluster shower shape and charge particle veto cuts. At large photon p_T (≈ 10 GeV/c in the PbSc), clusters from π^0 photon pairs start to overlap. Nearly all of such merged clusters, as well as other sources of hadron contamination, have an anomalous shower shape, and thus are removed from the analysis.

Charged hadrons are detected with the PHENIX tracking system [36] which employs a drift chamber in each arm, spanning a radial distance of 2.0–2.4 m from the beam axis, and a set of pixel pad chambers (PC1) situated directly behind them. The momentum resolution was determined to be $\delta p/p = 0.7\% \oplus 1.0\% p$ where p is measured in GeV/c. Secondary tracks from decays and conversions are suppressed by matching tracks to hits in a second pad chamber (PC3) at a radial distance of ~ 5.0 m. Track projections to the EMCal plane are used to veto photon candidates resulting from charged hadrons that shower in the EMCal.

The data used in this analysis consist of approximately 533×10^6 photon-triggered events from the 2005 and 2006 $p + p$ data sets. The total recorded integrated luminosities during these runs were 3.8 (2005) and 10.7 (2006) pb^{-1}, respectively. Events were obtained with an EMCal-based photon trigger, described in [37], which was over 90% efficient for events with a photon or π^0 in the range of energy used in this analysis.

B. π^0 and η reconstruction

The background for the present analysis consists of correlated decay photon-hadron pairs. In order to measure this background, π^0 and η mesons are reconstructed in the 2-γ channel, which together are responsible for approximately 95% of the decay photons. The invariant mass windows for π^0 and η mesons are 120–160 and 530–580 MeV/c^2, respectively, as shown in Fig. 3. The rate of combinatorial photon pairs is reduced by only considering photons of energy >1 GeV.

As discussed in the next section, jet correlations of decay photon *trigger* particles with charged hadron *partner* particles are estimated from those of their parent mesons. The quantity of interest is the per-trigger yield, Y. For the π^0, for example, the per-trigger yield, Y_π, is the number of π^0-hadron pairs divided by the number of π^0 triggers. For the given photon selection, the effect of combinatorial pairs on the measured per-trigger yield was evaluated with PYTHIA to be $<2\%$. The smallness of the effect is due both to the small combinatorial rate itself as well as the
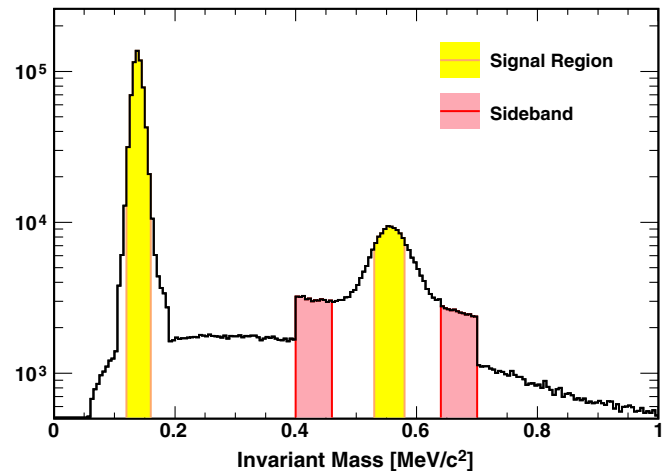
FIG. 3 (color online). Diphoton invariant mass distribution for pairs of $5 < p_T < 15$ GeV/c demonstrating π^0 and η reconstruction. The signal and sideband regions are indicated. Offline event filtering cuts are responsible for the features at 0.105, 0.185, 0.4 and 0.7 GeV/c^2.

similarity of correlations from falsely matched photons, most of which are themselves from π^0 decay, to the true π^0 correlations.

In contrast, reconstruction of the η meson has a much smaller signal-to-background of 1.4–1.6, depending on the p_T selection. In this case, the per-trigger yield of the combinatorial photon pairs is estimated from photon pairs with invariant mass in the sideband ranges of 400–460 and 640–700 MeV/c^2, beyond 3σ of the η peak. The procedure for subtracting this combinatorial contribution is discussed in [28] and gives rise to a 10% systematic uncertainty on the η per-trigger yields.

III. SUBTRACTION OF DECAY γ-HADRON CORRELATIONS

A. Statistical subtraction

A direct photon is defined here to be any photon not from a decay process including those from parton-to-photon fragmentation. The relative contribution of direct and decay photons is expressed in terms of the quantity R_γ, where $R_\gamma \equiv$ (number of inclusive photons)/ (number of decay photons). This quantity has been determined in the course of the measurement of the direct photon cross section in $\sqrt{s} = 200$ GeV $p + p$ collisions presented in [33] and its values are given in Table I.[2] In [28] the yield of charged hadrons per direct photon trigger was estimated by a statistical subtraction according to

$$Y_{\text{direct}} = \frac{1}{R_\gamma - 1}(R_\gamma Y_{\text{inclusive}} - Y_{\text{decay}}), \quad (1)$$

where the trigger particles in the per-trigger yields are inclusive photons, decay photons and direct photons as indicated.

The contribution of decay photons to the inclusive photon-hadron correlations is determined by weighting the measured π^0 (Y_π) and η (Y_η) correlations by their probability to contribute to a given Y_{decay} bin. For a given π^0 distribution the number of decay photons from π^0 in the decay photon bin of ($a < p_T^\gamma < b$) is given by

$$N_{\gamma(\pi)}(a < p_T^\gamma < b) = \int_a^b \epsilon_\gamma(p_T^\gamma, p_T^\pi) \cdot \mathcal{P}_\pi(p_T^\gamma, p_T^\pi)$$
$$\cdot \epsilon_\pi^{-1}(p_T^\pi) \cdot N_\pi(p_T^\pi) dp_T^\pi. \quad (2)$$

$\mathcal{P}_\pi(p_T^\gamma, p_T^\pi)$ is the decay probability density for a π^0 of p_T^π to decay into a photon of p_T^γ. ϵ_γ and ϵ_π are the single decay photon and π^0 reconstruction efficiency, respectively. The dependence of ϵ_γ on p_T^π is due to cluster merging at high p_T. For brevity, we define the efficiency corrected decay probability density:

---

[2]Note that the values of R_γ are not corrected for efficiency losses due to cluster merging.

TABLE I. R_γ and its effective values for the photon sample with tagging implemented (R_γ^{miss}) and the sample with tagging and isolation implemented (R_γ^{iso}).

p_T (GeV/c)	R_γ	R_γ^{miss}	R_γ^{iso}
5–7	1.19 ± 0.06	1.32 ± 0.11	1.38 ± 0.12
7–9	1.33 ± 0.05	1.67 ± 0.13	1.92 ± 01.4
9–12	1.54 ± 0.05	2.22 ± 0.18	2.87 ± 0.22
12–15	1.80 ± 0.11	2.69 ± 0.36	4.02 ± 0.50

$$P_\pi(p_T^\gamma, p_T^\pi) \equiv \epsilon_\gamma(p_T^\gamma, p_T^\pi) \cdot \mathcal{P}_\pi(p_T^\gamma, p_T^\pi) \cdot \epsilon_\pi^{-1}(p_T^\pi). \quad (3)$$

For a finite π^0 sample the integral in Eq. (2) becomes a sum and the per-trigger yield of decay photons from π^0 is calculated according to

$$Y_{\gamma(\pi)} = \frac{\sum_{N_\pi} P(p_T^\gamma, p_T^\pi) N_{\pi-h}}{\sum_{N_\pi} P(p_T^\gamma, p_T^\pi) N_\pi}, \quad (4)$$

where the p_T limits of the bins have been made implicit for brevity. For a perfect detector, P is calculable analytically. A Monte Carlo (MC) generator implements the PHENIX acceptance and uses Gaussian smearing functions to simulate detector resolution according to the known EMCal energy and position resolution. Occupancy effects give rise to an additional smearing of the π^0 and η invariant masses. This effect is included in the MC by tuning the resolution parameters to match the π^0 peak widths observed in data. The uncertainty on the decay photon mapping procedure, including the effect of combinatorial photon pairs in the π^0 matching window, was evaluated in PYTHIA to be 2%. This procedure is described in more detail in [28].

Once the decay photon correlations for π^0 and η triggers have been obtained, they are combined according to

$$Y_{\text{decay}} = (1/\delta_{\gamma(\pi)})Y_{\gamma(\pi)} + (1 - 1/\delta_{\gamma(\pi)})Y_{\gamma(\eta)}. \quad (5)$$

The quantity $\delta_{\gamma(\pi)}$ is the ratio of the total number of decay photons to the number of decay photons from π^0. Its value was estimated to be 1.24 ± 0.05 [33]. Inefficiencies in the detection of photons from π^0 decay increase the $\delta_{\gamma(\pi)}$ slightly, giving a value of 1.28 for decay photons in the range 12–15 GeV/c. Equation (5) effectively assigns the same per-trigger yield to the heavier mesons (ω, η', ϕ, ...) as for η triggers. This assumption was studied in PYTHIA and found to influence Y_{decay} at the level of 2%. The total systematic uncertainty on the decay photon-associated yields contains contributions from the η sideband subtraction, the value of $\delta_{\gamma(\pi)}$, the effect of hadrons heavier than η and the MC decay photon mapping procedure, in approximately equal parts.

The per-trigger yields are corrected for the associated charged hadron efficiency using a GEANT simulation of the PHENIX detector. The quoted yields correspond to a detector with full azimuthal acceptance and $|\eta| < 0.35$ cov-

erage. No correction is applied for the $\Delta\eta$ acceptance of pairs. A p_T-independent uncertainty of 8% was assigned to the charged hadron efficiency.

B. Decay photon tagging

The statistical and systematic uncertainties of the direct photon correlation measurement may be improved by event-by-event tagging of decay photons. It is not possible, however, to remove all decay photons due the finite acceptance and efficiency for parent meson reconstruction. The remainder must be subtracted according to the statistical method described in the preceding section. Photons are tagged when a partner photon of $p_T > 500$ MeV/c is detected such that the pair falls in an invariant mass window of 108–165 or 500–600 GeV/c^2. In what follows, all such tagged photon pairs are presumed to have been correctly identified as coming from the same meson parent. For the η meson the rate of combinatorial pairs is significant and is subtracted using the sidebands.

Letting the notation *tag* denote photons which have been tagged as coming from decay sources and the notation miss denote decay photons which could not be tagged, this residual decay component can be statistically subtracted analogously to Eq. (1) according to

$$Y_{\text{direct}} = \frac{1}{R_\gamma^{\text{miss}} - 1} \cdot (R_\gamma^{\text{miss}} Y_{\text{inclusive-tag}} - Y_{\text{decay}}^{\text{miss}}). \quad (6)$$

$Y_{\text{inclusive-tag}}$ is simply the per-trigger yield of all photons remaining in the sample after tagged decay photons are removed. The effective R_γ for the sample is

$$R_\gamma^{\text{miss}} \equiv \frac{N_{\text{inclusive}} - N_{\text{tag}}}{N_{\text{decay}} - N_{\text{tag}}} = \frac{R_\gamma}{1 - \epsilon_{\text{decay}}^{\text{tag}}} \frac{N_{\text{inclusive}} - N_{\text{tag}}}{N_{\text{inclusive}}}, \quad (7)$$

where the tagging efficiency, $\epsilon_{\text{decay}}^{\text{tag}}$, is $N_{\text{tag}}/N_{\text{decay}}$. $\epsilon_{\text{decay}}^{\text{tag}}$ varies from 0.43 in the 5–7 GeV/c bin to 0.53 in the 12–15 GeV/c bin.

In order to determine $Y_{\text{decay}}^{\text{miss}}$, we define a decay photon probability density P^{miss} in which the decay photon tagging is performed in the Monte Carlo simulation in the same manner as in the data. Figure 4 shows decay probability as a function of π^0 p_T for photons in the range $5 < p_T^\gamma < 7$ GeV/c [i.e., $\int_5^7 P(p_T^\pi, p_T^\gamma) dp_T^\gamma$] with and without the decay photon tagging applied. The curves should be interpreted as the probability (normalized up to $\pi^0 p_T = 20$ GeV/c) for a π^0 to decay into a 5–7 GeV/c photon in PHENIX acceptance as a function of π^0 p_T. The effect of the tagging is most pronounced in this lowest decay photon p_T bin because the opening angle between the decay photons is largest. Photons which pass the tagging cut are typically closer to the parent π^0 p_T than in the case when no tagging was applied.

The subtraction procedure defined above assumes that all tagged photons were paired correctly. A systematic
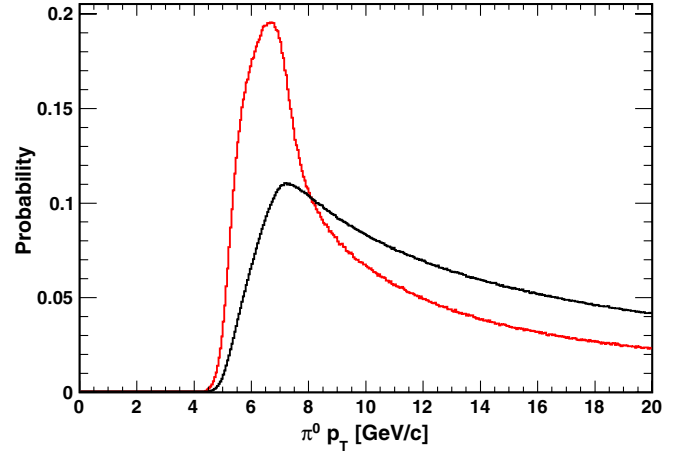
FIG. 4 (color online). The decay probability (normalized by area up to $p_T^\pi = 20$ GeV/c) for a π^0 to decay into a photon with $5 < p_T < 7$ GeV/c as a function of p_T^π with tagging (red line) and without tagging (black line).

uncertainty is assigned to account for the possibility that direct photons are falsely tagged by accidental combination with a decay photon. The rate of false tagging is estimated from the combinatorial background level determined from fits to the invariant mass distributions and is determined to be as large as 5% for the highest p_T^{trig} selection. The direct photon contribution to the falsely matched sample is assumed to be the same as in the absence of photon tagging (i.e., given by R_γ) and the total size of the direct photon contribution is taken as the systematic uncertainty.

C. Photon isolation

In order to further reduce the decay photon background one may impose an isolation requirement, as direct photons are expected to be largely produced without much associated hadronic activity. Such a requirement has the additional benefit of partially suppressing the fragmentation component. The isolation criterion employed in the present analysis is that the sum of the momenta of charged tracks and the energy of photon clusters inside a cone of radius 0.3 centered around the photon direction is less 10% of its energy. The cone size is limited by the size of the PHENIX aperture which spans 0.7 units of pseudorapidity. For photons near the edge of the detector the isolation cone lies partially outside of the PHENIX acceptance. In order to reduce the impact of the acceptance on the photon isolation, fiducial cuts are applied such that photons are required to be ~ 0.1 rad from the edge of the detector in both η and ϕ.

As was the case for decay photon tagging, a residual decay component must be statistically subtracted after the isolation cuts have been applied. The per-trigger yield of isolated direct photon is obtained according to

$$Y_{\text{direct}}^{\text{iso}} = \frac{1}{R_\gamma^{\text{iso}} - 1} (R_\gamma^{\text{iso}} Y_{\text{inclusive-tag}}^{\text{iso}} - Y_{\text{decay}}^{\text{iso}}). \qquad (8)$$

Note that the label *iso* (*niso*) denotes photons which are both isolated (nonisolated) and were not removed by the tagging cuts. The value of R_γ corresponding to the photon sample after both types of event-by-event cuts is

$$R_\gamma^{\text{iso}} \equiv \frac{N_{\text{inclusive}} - N_{\text{decay}}^{\text{tag}} - N_{\text{inclusive}}^{\text{niso}}}{N^{\text{decay}} - N_{\text{decay}}^{\text{tag}} - N_{\text{decay}}^{\text{iso}}}$$

$$= \frac{R_\gamma}{(1 - \epsilon_{\text{decay}}^{\text{tag}})(1 - \epsilon_{\text{decay}}^{\text{niso}})} \frac{N_{\text{inclusive}} - N_{\text{tag}} - N_{\text{isolated}}}{N_{\text{inclusive}}}.$$

$$(9)$$

The efficiency with which the isolation cut removes decay photons, $\epsilon_{\text{decay}}^{\text{niso}}$, is not known *a priori*, since an unknown fraction of the nonisolated photons are direct. In order to evaluate the isolation efficiency we apply the isolation cut at the level of the parent mesons and use the decay probability functions to map the effect to the daughter photon p_T. For the example of the π^0,

$$\epsilon_{\gamma(\pi)}^{\text{niso}} \equiv \frac{N_{\gamma(\pi)}^{\text{niso}}(p_T^\gamma)}{N_{\gamma(\pi)}^{\text{iso}}(p_T^\gamma) + N_{\gamma(\pi)}^{\text{niso}}(p_T^\gamma)}$$

$$= \left(1 + \frac{\sum_\pi P_\pi^{\text{miss}}(p_T^\pi, p_T^\gamma) \cdot N_\pi^{\text{iso}}(p_T^\pi)}{\sum_\pi P_\pi^{\text{miss}}(p_T^\pi, p_T^\gamma) \cdot N_\pi^{\text{niso}}(p_T^\pi)} \right)^{-1}. \qquad (10)$$

We have implicitly exploited the fact that the tagging probability is independent of the isolation requirement. $\epsilon_{\gamma(\pi)}^{\text{niso}}$ varies from 0.4 in the 5–7 GeV/c bin to 0.48 in the 12–15 GeV/c bin.

The per-trigger yield of isolated (and tagged) π^0 decay photons can be calculated according to

$$Y_{\gamma(\pi)}^{\text{iso}} = \frac{\sum_{N_\pi} P_\pi^{\text{miss}}(p_T^\gamma, p_T^\pi) N_{\pi-h}^{\text{iso}}}{\sum_{N_\pi} P_\pi^{\text{miss}}(p_T^\gamma, p_T^\pi) N_\pi^{\text{iso}}}. \qquad (11)$$

Azimuthal correlations for inclusive and decay photons for $9 < p_T^{\text{trig}} < 12$ and $2 < p_T^{\text{assoc}} < 5$ GeV/c are shown in Fig. 5. Also shown are the correlations after the tagging and isolation + tagging cuts have been applied. The tagging causes a reduction in the near-side yield of inclusive photons confirming that direct production is subsequently enhanced. The decay photon-associated yield is also smaller after tagging, due to the fact that the remaining photons have a smaller mean p_T, as can be ascertained from the decay probability function shown in Fig. 4. The isolation cut causes a further reduction in the yields, driven by the fact that the fraction of the jet momentum carried by the trigger is larger for isolated photons. Table I shows the R_γ and its effective values for the tagged and tagged + isolated samples.
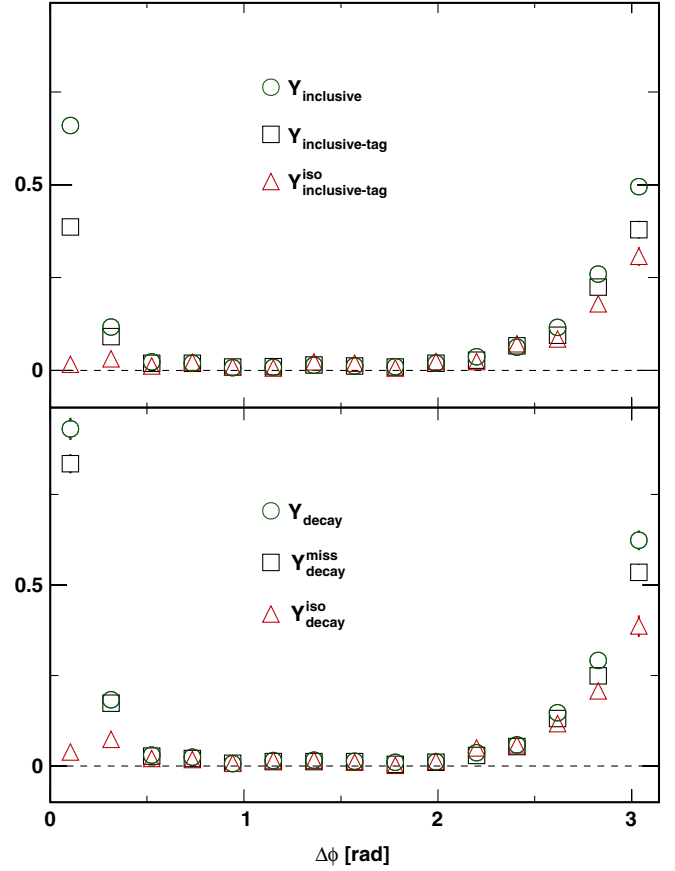
FIG. 5 (color online). Per-trigger yields for inclusive (top panel) and decay photons (bottom panel) with no event-by-event cuts, with decay photon tagging and with decay photon tagging and the isolation cut. The systematic uncertainties on the decay photon-triggered yields are not shown.

IV. RESULTS

A. Azimuthal correlations

Essential features of dijet or $\gamma +$ jet production are evident in azimuthal two-particle correlations. Figure 6 shows the per-trigger yields of associated charged hadrons as function of $\Delta\phi$ for π^0, direct photon (using decay photon tagging) and isolated direct photon triggers. The strong near-side correlation for π^0 triggers is largely absent for direct photon triggers as expected from a sample dominated by photons produced directly in the hard scattering. On the away side the direct photon-triggered yields are generally smaller than for π^0 triggers. Note that the error bars on the direct photon yields, which are from R_γ and from the decay photon yields, vary bin-to-bin depending on the relative values of $Y_{\text{inclusive}}$ and Y_{decay}. The 8% normalization uncertainty on the charged hadron yields is not shown on this plot and all those which follow.

B. Near-side correlations

The use of $\gamma +$ jet events, whether to calibrate the energy of the away-side jet in $p + p$ collisions or to study
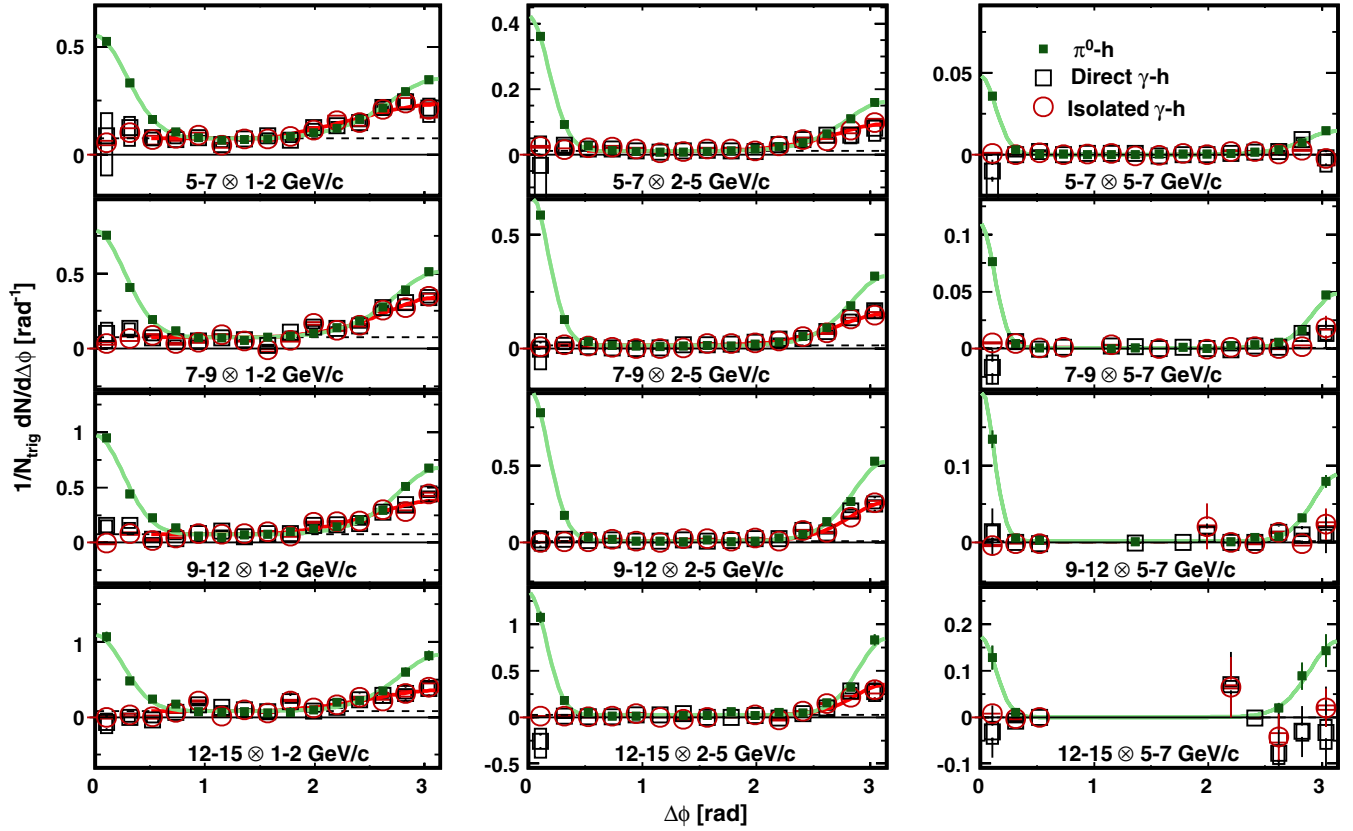
FIG. 6 (color online).   Yield per trigger of charged hadrons associated with π^0, direct and isolated direct photons triggers as a function of $\Delta\phi$. The lines correspond to fits which are described in Sec. IV E. The constant level, which estimates the contribution from the underlying event, is shown as a dashed line (only visible in the lower p_T^{assoc} bins).

its energy loss in nuclear collisions, relies on a detailed understanding of photons produced in jet fragmentation, which may be considered a background in this regard. Evidence of fragmentation photons may be observed indi-

FIG. 7 (color online).   The ratio of the direct photon to π^0 near-side ($\phi < \pi/2$) associated yields as a function of p_T^{assoc}. The points are placed according to $\langle p_T^{assoc} \rangle$ for the isolated direct photon-triggered sample.

rectly via near-side correlations of direct photon-hadron pairs. Figure 7 shows the ratio of the near-side yield of direct photon triggers to that of π^0 triggers for various p_T selections. The ratio is generally consistent with zero, albeit within fairly larger uncertainties. Such larger uncertainties on the near-side direct photon per-trigger yields are due to the large near-side associated yields for inclusive and decay photon triggers compared to the small difference between them.

The ratio Y_{direct}/Y_{π^0} is not a direct measurement of the relative contribution of fragmentation photons to the direct photon sample. This quantity is sensitive to both the overall contribution from fragmentation photons as well as the difference between parton-to-photon and parton-to-π^0 fragmentation functions and possibly a different number of quark vs gluon jets in the π^0 triggered and photon-triggered samples. As an illustrative example, if one assumes that the photon and π^0 fragmentation functions are similar in shape, it is reasonable to fit the ratio of the per-trigger yields to a constant value as a function of p_T^{assoc}. The results of such fits, shown in Table II, show that above 7 GeV/c the near-side yield associated with direct photons is constrained to be smaller than 15% of the π^0 associated yields. It should be emphasized that although such an observation is compatible with a small yield of fragmenta-

TABLE II. Ratio of constant fits to the near side yields as a function of p_T^{assoc} using isolated direct photon triggers to the same quantity using π^0 triggers.

p_T^{trig} (GeV/c)	Ratio from fit	Stat.	Syst.
5–7	0.01	0.04	+0.26–0.46
7–9	−0.03	0.04	+0.12–0.16
9–12	0.04	0.04	+0.07–0.09
12–15	−0.16	0.07	+0.14–0.17

tion photons, it may also reflect the different shape of the fragmentation function into photons compared to the fragmentation function into neutral pions. Similar results were obtained in $p + p$ collisions at $\sqrt{s} = 62.4$ GeV at the CERN-ISR [38,39].

C. Hard scattering kinematics using x_E and p_{out}

Because of the effects of hadronization, we do not have direct access to the parton kinematics and therefore can measure neither the fragmentation functions nor the magnitude of the k_T effect directly. However, to the extent that the LO Compton scattering process (see Fig. 1) dominates, direct photons may be considered to play the role of the hard-scattered parton. For both the case of isolated photon and π^0 triggered correlations we construct a simple model to extract the parton-level kinematics from the data, as described in the next section. To facilitate the interpretation of the data we choose a set of observables which are appropriately sensitive to the quantities of interest.

The fragmentation function is not directly measurable via two-particle correlations since the jet momentum is not determined. If the near-side jet p_T were fixed by that of the trigger particle and the jets were balanced, one could measure the fragmentation function of the away-side jet by measuring the associated yield as a function of the partner p_T. For the case of dihadron correlations, however, the Q^2 of the hard scattering varies with both the trigger and partner p_T selection, which are both jet fragments [16]. Direct photon triggers, on the other hand, should provide a nearly monoenergetic sample of jets for fixed photon p_T. The quantity $\hat{x}_h$ measures the transverse momentum imbalance between the trigger and associated parton:

$$\hat{x}_h \equiv \hat{p}_T^{\text{assoc}} / \hat{p}_T^{\text{trig}}, \qquad (12)$$

where the hat symbol denotes partonic level quantities. At LO $\hat{x}_h = 1$, but may deviate from unity due to the k_T effect. Given a falling $\hat{p}_T$ spectrum, $\hat{x}_h$ is typically less than one due to the trigger bias.

The quantity x_E measures the p_T balance between the trigger and associated particles [40]. It is defined in analogy to the fragmentation function variable z by substituting the the p_T of the trigger particle for that of the jet and taking the projection of the associated particle onto the trigger axis in the azimuthal plane:
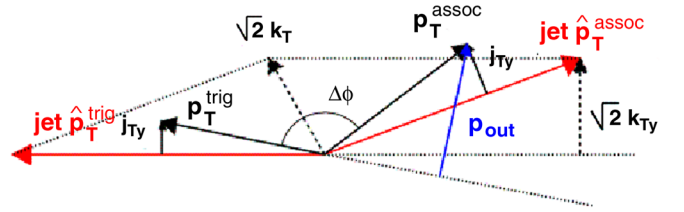
FIG. 8 (color online). A diagram showing the kinematics underlying the measurement of jet correlations between back-to-back particles, adapted from [16].

$$x_E \equiv -\frac{\vec{p}_T^{\text{trig}} \cdot \vec{p}_T^{\text{assoc}}}{|p_T^{\text{trig}}|^2} = -\frac{|p_T^{\text{assoc}}|}{|p_T^{\text{trig}}|} \cos\Delta\phi. \qquad (13)$$

For $p_T^{\text{trig}} \approx \hat{p}_T^{\text{trig}}$ (which is not the case for jet fragments measured at fixed p_T^{trig}), the x_E distribution approximates the fragmentation function, $D(z)$. Hence, the x_E distribution for direct photon triggers should scale with p_T^{trig}, in the same way as the fragmentation functions approximately scale with Q^2.

Beyond LO pQCD, the outgoing parton pair may acquire a net p_T as depicted in Fig. 8. The pair may acquire a net momentum along the both the dijet axis and orthogonal to it. At the hadron level, the kinematics along the jet axis are dominated by the effect of jet fragmentation. The k_T effect is therefore best observed by measuring the momentum of jet fragments in the direction orthogonal to the parton pair. Again using the trigger particle direction as a proxy for that of the parton, we define $\vec{p}_{\text{out}}$ as a vector transverse to p_T^{trig} of magnitude

$$|p_{\text{out}}| = |p_T^{\text{assoc}}| \sin\Delta\phi. \qquad (14)$$

p_{out} also contains a contribution from j_T which is the momentum transverse to the jet axis imparted to the jet fragment in the course of the parton showering process. Note that the presence of $|p_T^{\text{assoc}}|$ in p_{out} implies a dependence on the fragmentation function of the away-side jet. Similarly the longitudinal (along the dijet axis) component of $\vec{k}_T$ can play a role in the x_E distributions. Such a mixing of longitudinal and transverse effects is an unavoidable consequence of hadronization.

D. x_E Distributions

Figure 9 shows the away-side ($\Delta\phi > \pi/2$) charged hadron yield per trigger as a function of x_E for both π^0 and isolated direct photon triggers. The isolated direct photon-triggered data are obtained by the same procedure outlined in Sec. III that was used to obtain the $\Delta\phi$ distributions presented in the previous section. The isolated direct photon x_E distributions are significantly steeper than those of π^0. This is to be expected because, modulo the k_T smearing, the the x_E distribution opposite to an isolated direct photon should be the fragmentation function of the outgoing parton, predominantly the quark from the
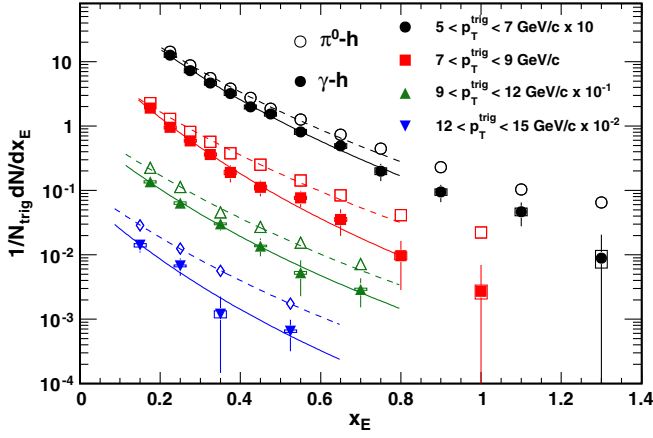
FIG. 9 (color online). Away-side charged hadron yield per π^0 trigger (open symbols) and isolated direct photon trigger (closed symbols) as a function of x_E, which is equivalent to z_T in the collinear limit $\cos(\Delta\phi) = 1$. The lines represent fits to the modified Hagedorn function described in the text.

Compton diagram (Fig. 1), with a small gluon admixture from the annihilation diagram.

The x_E distributions have been fit using a modified Hagedorn function defined by

$$\frac{dN}{dx_E} \approx N(n-1)\frac{1}{\hat{x}_h}\frac{1}{(1+\frac{x_E}{\hat{x}_h})^n}, \quad (15)$$

where n is the power-law dependence of the inclusive invariant π^0 p_T spectrum. This functional form was shown to describe the π^0 triggered x_E distribution given the following simplifying assumptions: The hadron is assumed to be collinear with the parton direction, i.e., $\cos\Delta\phi \approx 1$ in Eq. (13), the underlying fragmentation functions ($D(z)$) are assumed to take an exponential form and $\hat{x}_h$ is taken to be constant as a function of x_E. The fit was found to perform reasonably well for the range below $x_E \lesssim 0.8$. The results of the fits in this range are shown in Table III. The χ^2 values are rather large, particularly at low π^0 p_T, indicating that the data are not perfectly described by the modified Hagedorn function, which is perhaps not surprising given the good statistical precision of the π^0 triggered data. By further restricting the range of the fit, one can obtain values of χ^2 per degree of freedom much closer to unity. For example, a fit to the $5 < p_T^{trig} < 7$ GeV/c for $0.3 < \hat{x}_h <$

TABLE III. Parameters of fits to the x_E distributions for π^0 triggers for $x_E < 0.8$.

p_T^{trig} (GeV/c)	N	$\hat{x}_h$	χ^2/DOF
5–7	1.25 ± 0.02	0.71 ± 0.01	145/7
7–9	1.19 ± 0.03	0.75 ± 0.01	75/7
9–12	1.22 ± 0.06	0.76 ± 0.03	18/4
12–15	1.33 ± 0.09	0.75 ± 0.05	0.05/2
5–15	1.24 ± 0.02	0.72 ± 0.01	262/26

TABLE IV. Parameters of fits to the x_E distributions for isolated direct photon triggers.

p_T^{trig} (GeV/c)	N	$\hat{x}_h$	χ^2/DOF
5–7	1.35 ± 0.14	0.60 ± 0.03	2/7
7–9	1.40 ± 0.24	0.51 ± 0.05	3/7
9–12	0.83 ± 0.18	0.66 ± 0.10	0.5/4
12–15	0.75 ± 0.24	0.60 ± 0.15	1.4/2
5–15	1.11 ± 0.07	0.63 ± 0.02	44/26

0.8 yields a χ^2 per degree of freedom of 17.5/5. However, the extended range of the fit allows for a better comparison with the photon-triggered data, whose poorer statistical precision necessitates fits over a larger range.

For the case of isolated direct photon triggers, Eq. (15) will not describe the x_E distribution of the away-side jet because it is assumed that the trigger particle is also the fragment of a jet. However, for a fixed value of n, Eq. (15) is a useful quantitative representation of the steepness of the x_E distribution via the parameter $\hat{x}_h$; a smaller value of $\hat{x}_h$ corresponds to a steeper distribution. Since the parameters n and $\hat{x}_h$ have physical meaning for π^0-hadron correlations, we keep the same value of $n = 8.1$ for the isolated-γ-hadron correlations so as to get a quantitative measure of the relative steepness of the isolated-γ-hadron x_E distribution compared to the π^0-h distribution. The results of the fits, shown in Table IV, confirm a steeper distribution for photon triggers where statistical precision allows.

The independence of the $\hat{x}_h$ values for π^0 as a function of p_T suggests that x_E scaling should hold for all the data combined. This is shown in the left panel of Fig. 10 in which all π^0 p_T selections are fit simultaneously. It is interesting to note that the failure of x_E scaling in a similar measurement (for lower p_T, 2–4 GeV/c) at the CERN-ISR
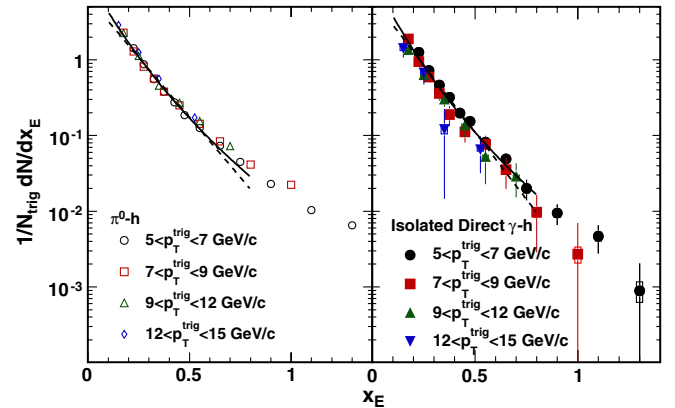
FIG. 10 (color online). x_E distributions for π^0 triggers and isolated direct photon triggers for all p_T^{trig} ranges combined. x_E is equivalent to z_T in the collinear limit $\cos(\Delta\phi) = 1$. The dashed lines and solid lines correspond to fits to exponential and modified Hagedorn [Eq. (15)] functions, respectively.
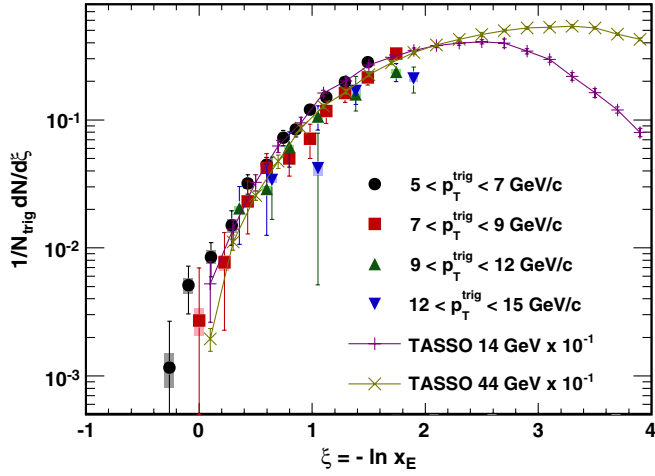
FIG. 11 (color online). $\xi = \ln 1/x_E$ distributions for isolated direct photon data for all p_T ranges combined compared to TASSO measurements in $e^+ e^-$ collisions at $\sqrt{s} = 14$ and 44 GeV.

[41], led to the concept of parton transverse momentum and k_T.

For isolated direct photon production, x_E scaling is important for a more fundamental reason. If the x_E distribution does indeed represent the fragmentation function of the opposite parton, then combining all the data (see Fig. 10) should, apart from NLO effects, give a universal distribution which is a reasonable representation of the quark fragmentation function [28].

Within the large errors, the x_E scaling appears to hold. Fits to both Eq. (15) and to a simple exponential are shown. The exponential fit (e^{-bx_E}) gives the value $b = 8.2 \pm 0.3$, with a χ^2 per degree of freedom of 48/26, which is in excellent agreement with the quark fragmentation function parameterized [16,28] as a simple exponential with $b = 8.2$ for $0.2 < z < 1.0$ and inconsistent with the value $b = 11.4$ for the gluon fragmentation function.

Another, recently more popular way [42] to look at the fragmentation function is to plot the distribution in the modified leading logarithmic approximation (MLLA) variable [43] $\xi \equiv \ln 1/z \approx \ln 1/x_E$ which is shown in Fig. 11. The present data compare well to the TASSO measurements [44] in $e^+ + e^-$ collisions which have been arbitrarily scaled by a factor of 10 to match the PHENIX data, which is reasonably consistent with the smaller acceptance of the present measurement. This again indicates consistency with a quark fragmentation function.

In Fig. 12 the isolated photon-triggered data is plotted as a function of z_T to compare to NLO calculations from [45]. The largest discrepancy occurs in the lowest p_T^{trig} bin where $\langle k_T \rangle$ should be closest to p_T^{trig}. Moreover, the deviation occurs for $p_T^{\text{assoc}} \ll p_T^{\text{trig}}$ where $\hat{p}_T^{\text{trig}}$ and $\hat{p}_T^{\text{assoc}}$ are most likely to be asymmetric and hence, the effect of k_T smearing is largest.
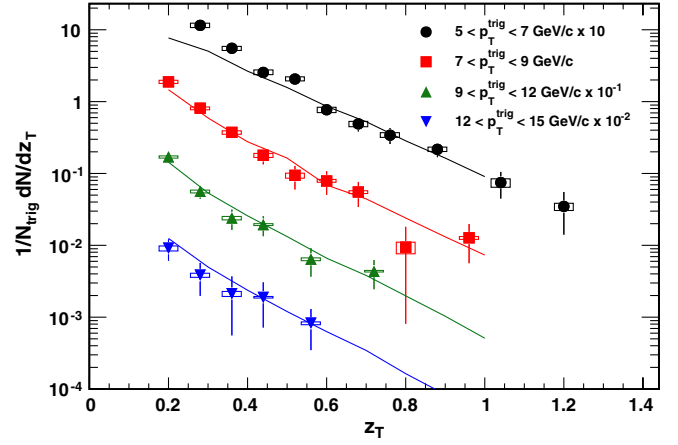
FIG. 12 (color online). z_T distributions for isolated direct photon triggers compared to NLO calculations from [45].

E. p_{out} distributions and $\sqrt{\langle |p_{\text{out}}|^2 \rangle}$

Figure 13 shows the p_{out} distributions for π^0 and isolated direct photons for the range of $2 < p_T^{\text{assoc}} < 10$ GeV/c. The π^0 distributions are fit with Gaussian functions, as well as by Kaplan functions. The Kaplan function is of the form $C(1 + p_{\text{out}}^2/b)^{-n}$, where C, n and b are free parameters. This function exhibits the same limiting behavior at small values of p_{out} as the Gaussian function and transitions to a power-law behavior as p_{out} becomes large. The tails of the distributions, above about 3 GeV/c, clearly exhibit a departure from the Gaussian fits. This may signal the transition from a regime dominated by multiple soft gluon emission to one dominated by radiation of a single hard gluon. The isolated direct photon data also show an excess above the fit, notably for the $7 < p_T^{\text{trig}} < 9$ GeV/c range. For values of p_{out} comparable to
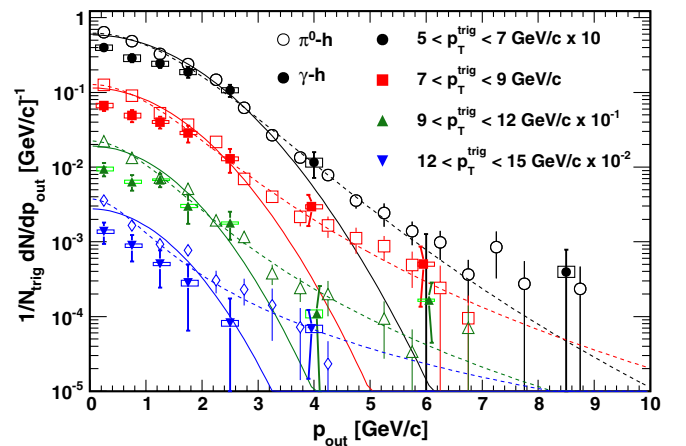
FIG. 13 (color online). p_{out} distributions for π^0 (open symbols) and isolated direct photon (filled symbols) triggers. The π^0 triggered distributions have been fit with both Gaussian (solid lines) and Kaplan (dashed lines) functions. Points with bent error bars have been shifted slightly for visibility.

p_T^{trig}, the direct photon data are consistent with zero yield. This is to be expected on kinematic grounds as the momentum of large angle radiation cannot exceed the jet momentum, which should be well-approximated by the photon momentum.

The value of $\sqrt{\langle |k_T|^2 \rangle}$ is determined by measuring $\sqrt{\langle |p_{\text{out}}|^2 \rangle}$. Rather than obtaining the values of $\sqrt{\langle |p_{\text{out}}|^2 \rangle}$ directly from the p_{out} distributions, fits to the azimuthal correlations are used, following the procedure described in [16,46]. In this method the contribution of the underlying event is parametrized by a $\Delta\phi$ independent contribution and the following fit function is used to determine the magnitude of p_{out} from the away-side jet width:

$$\frac{dN_{\text{real}}}{d\Delta\phi} = \frac{1}{N}\frac{dN_{\text{mix}}}{d\Delta\phi}$$
$$\cdot \left(C_0 + C_1 \cdot e^{-\Delta\phi^2/2\sigma_{\text{near}}^2} + C_2 \cdot \frac{dN_{\text{far}}}{d\Delta\phi}\Big|_{\pi/2}^{3\pi/2}\right),$$

$$(16)$$

where

$$\frac{dN_{\text{far}}}{d\Delta\phi}\Big|_{\pi/2}^{3\pi/2}$$
$$= \frac{-p_T^{\text{assoc}}\cos\Delta\phi}{\sqrt{2\pi\langle p_{\text{out}}^2\rangle}\,\text{Erf}(\sqrt{2}p_T^{\text{assoc}}/\sqrt{\langle p_{\text{out}}^2\rangle})}e^{(-|p_T^{\text{assoc}}|^2\sin^2\Delta\phi/2\langle p_{\text{out}}^2\rangle)}.$$

$$(17)$$

The underlying event level C_0, the near and away-side amplitudes C_1 and C_2 and $\sqrt{\langle |p_{\text{out}}|^2 \rangle}$ are free parameters.
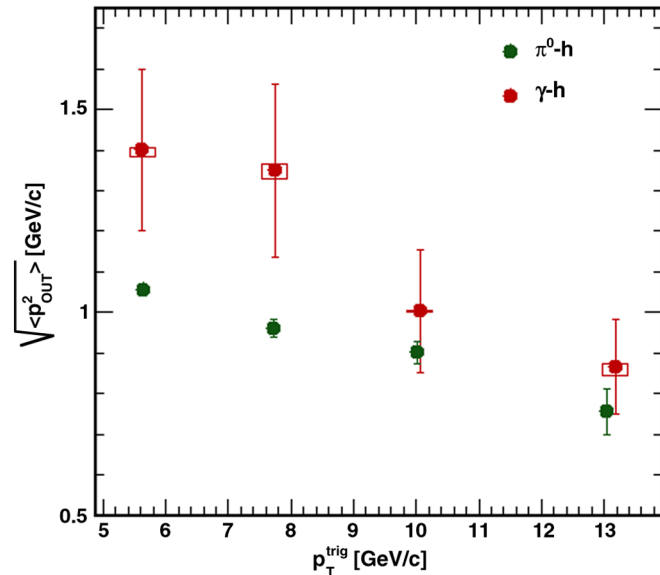
FIG. 14 (color online). $\sqrt{\langle |p_{\text{out}}|^2 \rangle}$ for π^0 and isolated direct photon triggers.

The fits to the $\Delta\phi$ distributions are shown in Fig. 6. Using the data for $p_T^{\text{assoc}} > 2$ GeV/c, we minimize the sensitivity to the underlying event whose level is indicated as a dashed line. C_0 is determined from the π^0 triggered correlations and treated as fixed for the direct photon correlations. Its value was confirmed to be equivalent for both trigger species in the range $1 < p_T^{\text{assoc}} < 2$ GeV/c where both sets of $\Delta\phi$ distributions could be reliably fit treating C_0 as a free parameter. The $\sqrt{\langle |p_{\text{out}}|^2 \rangle}$ values obtained from the fits are shown in Fig. 14. The width of the p_{out} distributions are found to decrease with p_T^{trig}. At the same value of p_T^{trig}, the isolated direct photon widths are larger than that of π^0, which is reasonable given that π^0 triggers on a larger jet momentum.

V. DISCUSSION AND INTERPRETATION

A. Leading order + Gaussian k_T smearing model

In order to interpret two-particle correlations of final-state particles in terms of properties of the hard-scattered partons, a model using the Born level pQCD cross sections and with a Gaussian k_T smearing was constructed (LO + k_T), similar to the model employed in [17]. Using this approach, the magnitude of the k_T effect is varied in the model until the measured values of $\sqrt{\langle |p_{\text{out}}|^2 \rangle}$ are reproduced. At leading order the differential cross section for back-to-back hadron production from a $2 \to 2$ scattering process ($p_1 + p_2 \to p_3 + p_4$) is

$$\frac{d^5\sigma}{dx_1 dx_2 d\cos\theta^* dz_3 dz_4}$$
$$= \sum_{a,b,c,d} f_a(x_1)f_b(x_2)\frac{\pi\alpha_s^2(Q^2)}{2\hat{s}}\hat{\sigma}_{a,b}(\cos\theta^*)D_c(z_3)D_d(z_4).$$

$$(18)$$

A Monte Carlo generator is used to throw flat distributions of particle pairs in x_1, x_2, θ^*, z_3 and z_4, where x is the fraction of the proton's momentum taken by the initial-state parton, θ^* is the polar scattering angle, and z is the fraction of the final-state parton taken by a fragment. For pairs which fall in the PHENIX pseudorapidity ($|\eta| < 0.35$) interval the right-hand side of Eq. (18) is used to weight the contribution of each particle pair. The expression consists of the angular component of the LO parton scattering cross section, $\hat{\sigma}$, for each parton flavor combination $a + b$ and the nonperturbative parton distribution functions (PDF), f, and fragmentation functions (FF), D. An equal number of all possible permutations of each parton flavor are thrown, neglecting charm and heavier quarks. The angular part of the parton scattering cross section, $\hat{\sigma}_{a,b}(\cos\theta^*)$, contains a numerical factor which weights each scattering process appropriately. $\hat{s}$ is the Mandelstam variable representing the square of the center-of-mass energy at the partonic level and is related

to the $p + p$ center-of-mass energy of $\sqrt{s} = 200$ GeV by $\hat{s} = x_1 x_2 s$. The amplitudes for dijet processes can be found in [47]. Direct photon-hadron correlations are also considered. The $\gamma + $ jet amplitudes can be found in [48]. In this case, $D(z_4)$ is taken to be a δ function at $z_4 = 1$ and the α_s^2 coupling becomes $\alpha_s \alpha_{\mathrm{EM}}$.

The PDFs and FFs are taken from global fit analyses. The PDFs used in this study are the CTEQ6 set [2] evaluated using NLO evolution which were obtained from the Durham HEP database [49]. Several fits to the FFs, KKP, AKK and DSS are tested with the Monte Carlo generator [5,50,51]. These parametrizations differ in the selection of data sets used in their fits. The KKP set relies solely on $e^+ e^-$ data while the recent AKK and DSS fits also employ data from deeply inelastic scattering and $p + p$ collisions. The use of these additional data sets enables the separation of the quark and antiquark FFs and provides much better constraints on the gluon FFs, although uncertainties for the gluon FFs remain large. Despite the recent progress, the AKK and DSS differ quite substantially in a number of observables and discrepancies exist between fits and certain data sets. Newer data sets and observables are required to further constrain the FFs. Of particular interest for studies of heavy-ion collisions is the region of low z where modifications of the FF by the dense QCD medium are expected. Whereas inclusive hadron cross sections are most sensitive to relatively large values of z (typically 0.7–0.8), two-particle correlations provide access to smaller values of z using an asymmetric p_T selection of the trigger and partner. Direct photons are ideally suited for this purpose due to the absence of near-side jet fragmentation effects at LO. However, higher order effects such as photon fragmentation and soft gluon emission must be constrained.

The k_T effect is modeled by introducing a Gaussian distributed boost of magnitude $|p_T^{\mathrm{pair}}| = \sqrt{2}|k_T|$ randomly oriented in the plane transverse to the incoming parton pair, i.e. the beam direction. The outgoing parton pair, which is back-to-back to leading order, hence acquire an acoplanarity and a momentum imbalance. In addition to k_T the hadrons also acquire some momentum relative to their parent parton direction, denoted by $\vec{j}_T$, from the parton showering process. The width of the j_T distribution is taken from measurements of π^0-hadron correlations and was determined to be $\sqrt{\langle |j_T|^2 \rangle} = 635$ MeV/c [46].

The Gaussian k_T smearing model has the advantage of simplicity compared to a more detailed calculation of the underlying jet kinematics and subsequent fragmentation. Although NLO calculations are available, modeling the k_T smearing would require care to avoid double-counting the contribution at NLO with that of soft gluon radiation. A self-consistent approach to doing so would require a fully resummed calculation for which generator level Monte Carlo simulations are not presently available. Although a Gaussian k_T smearing can be similarly tuned

in more sophisticated LO models such as PYTHIA, the LO + k_T model enables us to test various parametrizations of the fragmentation functions as opposed to using a model of the hadronization process.

It should be emphasized, however, that the Gaussian k_T smearing model does not take into account the full parton kinematics and hence, requires some care to avoid unphysical scenarios. The LO cross sections are divergent in the forward and/or backward directions and the gluon distribution becomes very large at low x. In the absence of k_T smearing these effects are irrelevant for production at midrapidity. However, for a Gaussian distributed k_T of fixed width there is a finite probability for a parton to be scattered at large angle, solely by virtue of receiving a large momentum kick from sampling the tail of the k_T distribution. Because of the largeness of the low x gluon distribution and the cross sections at small angle these soft partons would dominate the cross section. This is clearly an unphysical consequence of the k_T smearing procedure. The k_T boost is intended to simulate gluon emission which should clearly be bounded by the momentum of the parton from which it radiates. This requirement is enforced by imposing the that $|k_T| < x\sqrt{s}/2$. The calculation was found to be insensitive to the threshold.
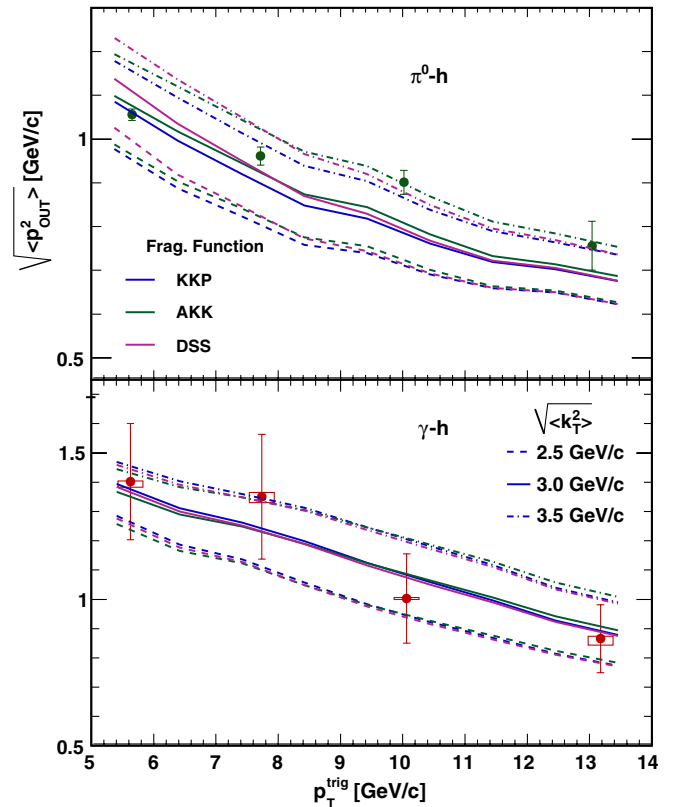
FIG. 15 (color online). $\sqrt{\langle |p_{\mathrm{out}}|^2 \rangle}$ compared to LO + k_T calculations for π^0 triggers (top panel) and isolated direct photon triggers (bottom panel).

B. Estimating the magnitude of the k_T effect

In order to determine the best value of $\sqrt{\langle|k_T|^2\rangle}$, $\sqrt{\langle|p_{\text{out}}|^2\rangle}$ is calculated from the model for several different values of $\sqrt{\langle|k_T|^2\rangle}$ and the results are compared to data. Figure 15 shows $\sqrt{\langle|p_{\text{out}}|^2\rangle}$ values as well as the LO + k_T calculation for several values of $\sqrt{\langle|k_T|^2\rangle}$ and several parametrizations of the FFs. The π^0 triggered data show that although the LO + k_T qualitatively reproduces the trend of the data, it does not perfectly reproduce the p_T^{trig} dependence of $\sqrt{\langle|p_{\text{out}}|^2\rangle}$. Additional effects not included in the LO + k_T smearing model may certainly be relevant at this level. At NLO effects such as the radiation of a hard gluon play a role. Alternatively, soft gluon radiation may not be perfectly described by a Gaussian smearing or may depend on the scattering process or the momentum exchange of the hard scattering.

The χ^2 per degree of freedom between data and model calculations are shown in Fig. 16. Direct photon triggers give a best value of $\sqrt{\langle|k_T|^2\rangle} \approx 3$ GeV/c. The best value for π^0 triggers is somewhat larger and depends on the choice of FF. This dependence arises from the effect of fragmentation on the near side and the larger fraction of gluon jets, for which the parametrizations differ.

Figure 17 shows $\sqrt{\langle|k_T|^2\rangle}$ as function of p_T^{trig} as calculated in the LO + k_T model for the best value of the input $\sqrt{\langle|k_T|^2\rangle}$ as determined from Fig. 16. The systematic error band indicates the dependence on the choice of FF parametrization. The value of $\sqrt{\langle|k_T|^2\rangle}$ may depend on p_T^{trig} since the trigger requirement may preferentially select events based on their k_T. For both the π^0 and photon-triggered samples, the value of $\sqrt{\langle|k_T|^2\rangle}$ depends on p_T^{trig}, and reaches values larger than the input, although the effect is only statistically significant for the π^0 triggered data. The val-
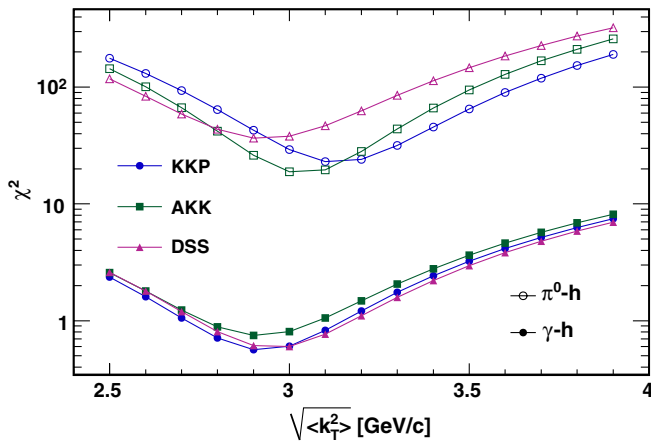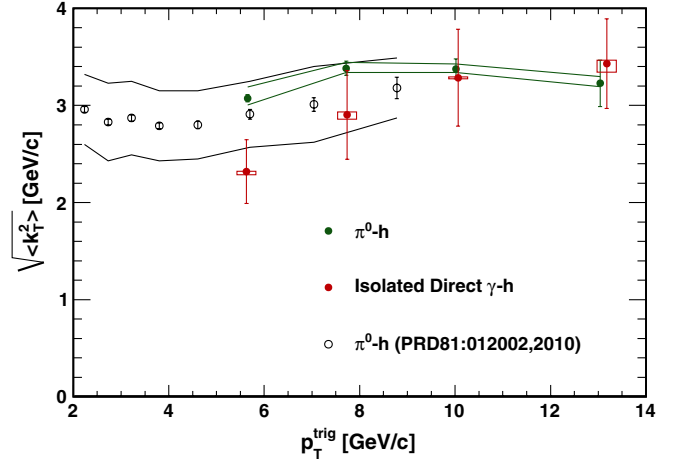
FIG. 17 (color online). $\sqrt{\langle|k_T|^2\rangle}$ as a function of p_T^{trig} for π^0 and isolated direct photon triggers. Also shown are $\pi^0 - h$ results using a different method [16].

ues of $\sqrt{\langle|k_T|^2\rangle}$ are generally larger for π^0 triggers, but within statistical uncertainties on the photon-triggered sample, the size of the k_T effect is of comparable magnitude.

C. Sensitivity of x_E distributions to the fragmentation functions

Using the value of $\sqrt{\langle|k_T|^2\rangle}$ which best matches the data, the shape of the x_E distribution can be calculated in the LO + k_T model, for each set of FFs, and compared to the data. Figure 18 (top panel) shows the slope parameter, $\hat{x}_h$, of the power-law fits to the x_E distributions for π^0 triggers shown in Fig. 9. Several calculations are shown. The KKP and DSS fits reproduce the shape of the data better than the AKK fit, which shows a much harder slope. The disparity amongst the calculations seems to contradict the claim in [16] that the x_E distribution for π^0 triggers is not sensitive to the overall shape of the FF. To test this assertion using the LO + k_T model, an exponential function was used for each flavor of FF. The slopes of the FFs were varied, using $D(z) \propto \exp(-8.2z)$ and $D(z) \propto \exp(-11.4z)$, to represent the quark and gluon FFs, respectively, as was done in [16]. Indeed one finds that the calculation is not very sensitive to the change in the slope parameter. This exercise does not, however, take into account that a change in the shape of the FF for an individual parton flavor may change not only the admixture of quark and gluon jets, but also the shape of the p_T distribution of hard-scattered partons, which is taken to be fixed in [16]. Since the PDF for the gluon is much different than for the quarks, the sensitivity of the x_E distribution to the parent parton composition of the π^0 triggered jets can be tested by removing gluon scattering processes from the calculation. To illustrate this, the slope resulting from using only the $q + q \rightarrow q + q$ processes with the DSS FFs is also shown in Fig. 18. A significantly

FIG. 16 (color online). χ^2 between the values of $\sqrt{\langle|p_{\text{out}}|^2\rangle}$ obtained in data and from MC calculation for π^0 and isolated direct photon triggers.
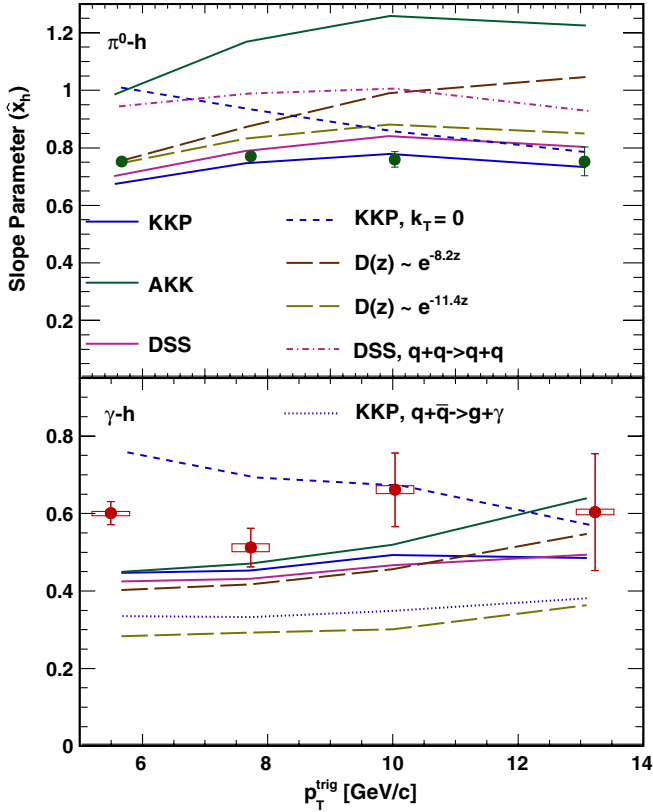
FIG. 18 (color online). Slope parameter $\hat{x}_h$ of fits to the x_E distributions shown in Fig. 9 for π^0 (top panel) and direct photon (bottom panel) triggers. The slopes are compared to various calculations using the LO + k_T model as discussed in the text.

harder slope is obtained, verifying that the x_E distribution depends on the parton species composition of the triggered jet sample. The effect of the k_T smearing on the shape of the x_E distribution was also investigated. Turning off the smearing results in a harder slope for smaller p_T^{trig}, which gradually disappears as p_T^{trig} becomes much larger than $\langle k_T \rangle$.

Figure 18 (bottom panel) shows the same comparison for isolated photon triggers. Here the calculation depends less strongly on the choice of FF parametrization due to the smaller contribution of the annihilation subprocess, $q + \bar{q} \rightarrow \gamma + g$, compared to the predominant $g + q \rightarrow \gamma + q$. In contrast to the π^0 triggered sample, the shape of the x_E distribution depends rather strongly on the shape of the overall FF as demonstrated by varying the slope parameter of the exponential parametrization. The magnitude of this effect is reproduced in a gluon jet sample, in which only the annihilation process is turned on. The distribution for the gluon jet sample is significantly steeper than the data, verifying that the sample is dominated by quark jet fragmentation. As for the π^0 triggered sample, the Monte Carlo x_E distribution becomes harder if the k_T smearing is turned off. Irrespective of the fit, the data in the $5 < p_T^{trig} <$
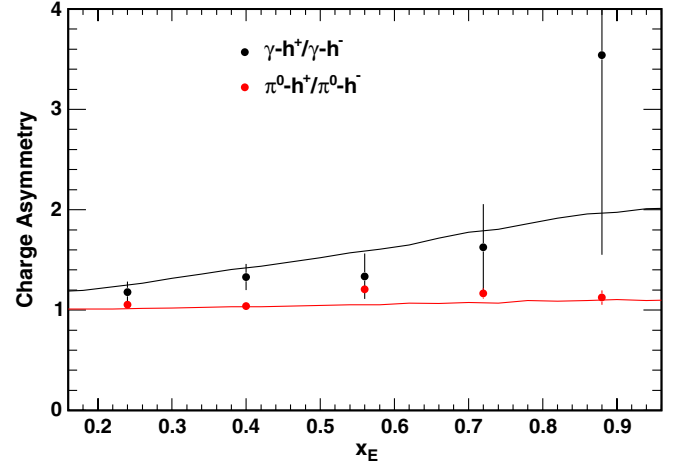
FIG. 19 (color online). Charge asymmetry of hadrons opposite isolated direct photon and π^0 triggers as a function of x_E and the corresponding calculations in the LO + k_T model using the DSS FFs.

7 GeV/c bin are incompatible with a model without k_T smearing, as a significant yield is observed at $x_E > 1$.

D. Charge asymmetry

The dominance of Compton scattering in direct photon production implies that the flavor distribution of valence quarks in the proton should be reflected in the away-side parton. Since there are twice as many up quarks as down and the amplitude depends on the electric charge of the quark, one expects an asymmetry of 8:1 in the number of up quark to down quark recoil jets from the Compton scattering of a valence quark and a gluon. One expects a dilution of this factor for several reasons, for example, creation of charge pairs in the course of the parton shower process, corrections from higher order processes such as photon fragmentation and a contribution from sea quarks. Nevertheless, a residual charge asymmetry should be apparent in the final-state hadrons. Figure 19 shows the ratio of positively to negatively charged hadrons ($R\pm$) on the away side of both π^0 and isolated direct photon triggers as a function of p_T^{assoc} along with calculations using the DSS FFs in the LO + k_T model with the best value of k_T as determined in Sec. V B. The π^0 triggered data show an $R\pm$ close to unity. On the other hand, an excess of positive charge is evident in the isolated direct photon-triggered yields. This supports the claim that the recoil jet is dominated by quark fragmentation. These results are in agreement with a previous measurement at $\sqrt{s} = 62.4$ GeV [38].

VI. CONCLUSIONS

A detailed understanding of jet fragmentation in $p + p$ collisions is a prerequisite for studies of possible medium modifications to the fragmentation functions by the QCD

medium at RHIC. To this end, this study provides baseline measurements of two-particle correlations from which to quantify these effects. Direct photon-triggered correlations were obtained by a combination of event-by-event identification, in the form of decay photon tagging and isolation cuts, and a subtraction of the residual decay photon-associated component. The measurement of near-side hadron production associated with inclusive direct photon (i.e., without isolation cuts) triggers shows no evidence for a large contribution from dijet processes, as might be expected from a large fragmentation photon component. The yield opposite isolated direct photons was found to be smaller than for π^0, consistent with the expectation of a smaller away-side jet momentum for fixed p_T^{trig}. Furthermore, the isolated direct photon-associated yields were steeper than for π^0 and demonstrated x_E scaling as one would expect if the distributions closely resemble the underlying charged hadron fragmentation function. As a function of p_{out}, the away-side yields for π^0 triggers show a Gaussian-like behavior at small values of p_{out}, whereas a harder, power-law like component emerges at large p_{out}. The tail component is interpreted to be due the emission of a hard gluon. The isolated direct photon-triggered distributions also appear to show evidence for a hard tail; however the data are consistent with zero yield when $p_{\text{out}} \gtrsim p_T^{\text{trig}}$, corresponding to the kinematic limit for LO photon production.

The results were further interpreted at the parton level using a simple model of LO pQCD incorporating a phenomenologically-motivated Gaussian k_T smearing. The hadron yields opposite isolated direct photons are shown to be directly sensitive to the fragmentation function of the away-side parton. In contrast, hadron triggered jets are sensitive only indirectly, due to the contribution of multiple subprocesses in the initial state, the relative contribution of which is sensitive to the gluon FFs. Furthermore, the shape of the distributions are shown to be compatible with the Compton scattering process $q + g \rightarrow q + \gamma$. The dominance of the Compton scattering process is further reinforced by the positive charge asymmetry observed opposite isolated direct photon triggers. Finally, the direct photon data are shown to be compatible with a $\sqrt{\langle |k_T|^2 \rangle}$ of about 3 GeV/c, which is of similar magnitude to that required by the π^0 triggered data, within uncertainties. Such a large momentum imbalance between the photon and the recoil jet is significant for studies of photon tagged jets in nuclear collisions in the kinematic regime currently accessible at RHIC.

[1] T. Ferbel and W. R. Molzon, Rev. Mod. Phys. **56**, 181 (1984).

[2] J. Pumplin *et al.*, J. High Energy Phys. 07 (2002) 012.

[3] P. Aurenche, R. Baier, M. Fontannaz, J. Owens, and M. Werlen, Phys. Rev. D **39**, 3275 (1989).

[4] W. Vogelsang and A. Vogt, Nucl. Phys. **B453**, 334 (1995).

[5] B. A. Kniehl, G. Kramer, and B. Potter, Nucl. Phys. **B597**, 337 (2001).

[6] B. Abbott *et al.* (D0 Collaboration), Nucl. Instrum. Methods Phys. Res., Sect. A **424**, 352 (1999).

[7] K. Ackerstaff *et al.* (OPAL Collaboration), Eur. Phys. J. C **2**, 39 (1998).

[8] L. Bourhis, M. Fontannaz, and J. P. Guillet, Eur. Phys. J. C **2**, 529 (1998).

[9] J. Alitti *et al.* (UA2 Collaboration), Phys. Lett. B **263**, 544 (1991).

[10] F. Abe *et al.* (CDF Collaboration), Phys. Rev. Lett. **73**, 2662 (1994).

[11] S. Abachi *et al.*, Phys. Rev. Lett. **77**, 5011 (1996).

[12] S. Chekanov *et al.* (ZEUS Collaboration), Phys. Lett. B **595**, 86 (2004).

[13] F. D. Aaron *et al.* (H1 Collaboration), Eur. Phys. J. C **54**, 371 (2008).

[14] R. P. Feynman, R. D. Field, and G. C. Fox, Nucl. Phys. **B128**, 1 (1977).

[15] G. Altarelli, R. K. Ellis, M. Greco, and G. Martinelli, Nucl. Phys. **B246**, 12 (1984).

[16] S. S. Adler *et al.* (PHENIX Collaboration), Phys. Rev. D **74**, 072002 (2006).

[17] L. Apanasevich *et al.*, Phys. Rev. D **59**, 074007 (1999).

[18] P. Aurenche, J. P. Guillet, E. Pilon, M. Werlen, and M. Fontannaz, Phys. Rev. D **73**, 094007 (2006).

[19] E. Laenen, G. Sterman, and W. Vogelsang, Phys. Rev. Lett. **84**, 4296 (2000).

[20] P. Stankus, Annu. Rev. Nucl. Part. Sci. **55**, 517 (2005).

[21] K. Adcox *et al.* (PHENIX Collaboration), Nucl. Phys. **A757**, 184 (2005).

[22] K. Adcox *et al.* (PHENIX Collaboration), Phys. Rev. Lett. **88**, 022301 (2001).

[23] S. S. Adler *et al.* (PHENIX Collaboration), Phys. Rev. Lett. **91**, 072301 (2003).

[24] S. S. Adler *et al.* (PHENIX Collaboration), Phys. Rev. Lett. **94**, 232301 (2005).

[25] B. G. Zakharov, JETP Lett. **80**, 617 (2004).

[26] R. J. Fries, B. Muller, and D. K. Srivastava, Phys. Rev. Lett. **90**, 132301 (2003).

[27] X.-N. Wang, Z. Huang, and I. Sarcevic, Phys. Rev. Lett. **77**, 231 (1996).

[28] A. Adare *et al.* (PHENIX Collaboration), Phys. Rev. C **80**, 024908 (2009).

[29] F. Arleo, Eur. Phys. J. C **61**, 603 (2009).

[30] K. Adcox *et al.* (PHENIX Collaboration), Nucl. Instrum. Methods Phys. Res., Sect. A **499**, 469 (2003).

[31] K. Adcox *et al.* (PHENIX Collaboration), Nucl. Instrum. Methods Phys. Res., Sect. A **499**, 489 (2003).

[32] L. Aphecetche *et al.* (PHENIX Collaboration), Nucl. Instrum. Methods Phys. Res., Sect. A **499**, 521 (2003).

[33] S. S. Adler *et al.* (PHENIX Collaboration), Phys. Rev. Lett. **98**, 012002 (2007).

[34] A. Adare *et al.* (PHENIX Collaboration), Phys. Rev. D **76**, 051106 (2007).

[35] S. S. Adler *et al.* (PHENIX Collaboration), Phys. Rev. C **75**, 024909 (2007).

[36] K. Adcox *et al.* (PHENIX Collaboration), Nucl. Instrum. Methods Phys. Res., Sect. A **499**, 489 (2003).

[37] S. S. Adler *et al.* (PHENIX Collaboration), Phys. Rev. Lett. **91**, 241803 (2003).

[38] A. L. S. Angelis *et al.* (CMOR Collaboration), Nucl. Phys. **B327**, 541 (1989).

[39] T. Akesson *et al.* (Axial Field Spectrometer Collaboration), Phys. Lett. **118B**, 178 (1982).

[40] P. Darriulat *et al.*, Nucl. Phys. **B107**, 429 (1976).

[41] M. Della Negra *et al.* (CERN-College de France-Heidelberg-Karlsruhe Collaboration), Nucl. Phys. **B127**, 1 (1977).

[42] N. Borghini and U. A. Wiedemann, arXiv:hep-ph/0506218.

[43] Y. L. Dokshitzer, V. A. Khoze, and S. I. Troian, Z. Phys. C **55**, 107 (1992).

[44] W. Braunschweig *et al.* (TASSO Collaboration), Z. Phys. C **47**, 187 (1990).

[45] H. Zhang, J. F. Owens, E. Wang, and X.-N. Wang, Phys. Rev. Lett. **103**, 032302 (2009).

[46] A. Adare *et al.* (PHENIX Collaboration), Phys. Rev. D **81**, 012002 (2010).

[47] B. L. Combridge, J. Kripfganz, and J. Ranft, Phys. Lett. **70B**, 234 (1977).

[48] H. Fritzsch and P. Minkowski, Phys. Lett. **69B**, 316 (1977).

[49] http://durpdg.dur.ac.uk/hepdata/pdf3.html.

[50] S. Albino, B. A. Kniehl, and G. Kramer, Nucl. Phys. **B803**, 42 (2008).

[51] D. de Florian, R. Sassot, and M. Stratmann, Phys. Rev. D **75**, 114010 (2007).